# 10SM

# Detection and Attribution of Climate Change: from Global to Regional

## Supplementary Material

**Coordinating Lead Authors:**
Nathaniel L. Bindoff (Australia), Peter A. Stott (UK)

**Lead Authors:**
Krishna Mirle AchutaRao (India), Myles R. Allen (UK), Nathan Gillett (Canada), David Gutzler (USA), Kabumbwe Hansingo (Zambia), Gabriele Hegerl (UK/Germany), Yongyun Hu (China), Suman Jain (Zambia), Igor I. Mokhov (Russian Federation), James Overland (USA), Judith Perlwitz (USA), Rachid Sebbari (Morocco), Xuebin Zhang (Canada)

**Contributing Authors:**
Magne Aldrin (Norway), Beena Balan Sarojini (UK/India), Jürg Beer (Switzerland), Olivier Boucher (France), Pascale Braconnot (France), Oliver Browne (UK), Ping Chang (USA), Nikolaos Christidis (UK), Tim DelSole (USA), Catia M. Domingues (Australia/Brazil), Paul J. Durack (USA/Australia), Alexey Eliseev (Russian Federation), Kerry Emanuel (USA), Graham Feingold (USA), Chris Forest (USA), Jesus Fidel González Rouco (Spain), Hugues Goosse (Belgium), Lesley Gray (UK), Jonathan Gregory (UK), Isaac Held (USA), Greg Holland (USA), Jara Imbers Quintana (UK), William Ingram (UK), Johann Jungclaus (Germany), Georg Kaser (Austria), Veli-Matti Kerminen (Finland), Thomas Knutson (USA), Reto Knutti (Switzerland), James Kossin (USA), Mike Lockwood (UK), Ulrike Lohmann (Switzerland), Fraser Lott (UK), Jian Lu (USA/Canada), Irina Mahlstein (Switzerland), Valérie Masson-Delmotte (France), Damon Matthews (Canada), Gerald Meehl (USA), Blanca Mendoza (Mexico), Viviane Vasconcellos de Menezes (Australia/Brazil), Seung-Ki Min (Republic of Korea), Daniel Mitchell (UK), Thomas Mölg (Germany/Austria), Simone Morak (UK), Timothy Osborn (UK), Alexander Otto (UK), Friederike Otto (UK), David Pierce (USA), Debbie Polson (UK), Aurélien Ribes (France), Joeri Rogelj (Switzerland/Belgium), Andrew Schurer (UK), Vladimir Semenov (Russian Federation), Drew Shindell (USA), Dmitry Smirnov (Russian Federation), Peter W. Thorne (USA/Norway/UK), Muyin Wang (USA), Martin Wild (Switzerland), Rong Zhang (USA)

**Review Editors:**
Judit Bartholy (Hungary), Robert Vautard (France), Tetsuzo Yasunari (Japan)

**This chapter supplementary material should be cited as:**
Bindoff, N.L., P.A. Stott, K.M. AchutaRao, M.R. Allen, N. Gillett, D. Gutzler, K. Hansingo, G. Hegerl, Y. Hu, S. Jain, I.I. Mokhov, J. Overland, J. Perlwitz, R. Sebbari and X. Zhang, 2013: Detection and Attribution of Climate Change: from Global to Regional Supplementary Material. In: Climate Change 2013: *The Physical Science Basis. Contribution of Working Group I to the Fifth Assessment Report of the Intergovernmental Panel on Climate Change* [Stocker, T.F., D. Qin, G.-K. Plattner, M. Tignor, S.K. Allen, J. Boschung, A. Nauels, Y. Xia, V. Bex and P.M. Midgley (eds.)]. Available from www.climatechange2013.org and www.ipcc.ch.

# Table of Contents

## 10.SM.1 Notes and Technical Details on Figures Displayed in Chapter 10

### Box 10.1, Figure 1

**a).** Observed global annual mean temperatures 1860–2012 relative to the 1880–1919 climatology from the Hadley Centre/Climatic Research Unit gridded surface temperature data set 4 (HadCRUT4) data set (coloured dots, with colours also indicating observed temperature) compared with Coupled Model Intercomparison Project Phase 3 (CMIP3)/CMIP5 ensemble mean response to anthropogenic forcing (orange), natural forcing (blue) and best-fit linear combination (black). CMIP series was obtained by a simple average over the models available for each year, with equal weight given to each model. Anthropogenic signal obtained by differencing historical from natural simulations. Anthropogenic and natural simulations are masked to correspond to observations following Jones et al. (2013 ) and Figure 10.1 and noise-reduced with 5-point running mean. To avoid smoothing out the volcanic signals, smoothing is not performed over years where the ensemble mean natural simulations decreases by more than 0.05°C.

**b).** Same as panel a), but plotting against CMIP ensemble mean anthropogenic warming instead of time. Note that the only change from Box 10.1 Figure 1 (a) is the location of points in the horizontal.

**c).** Same as panel b), but plotting observed annual mean temperatures against CMIP ensemble mean anthropogenic warming in one direction, and naturally forced temperature change in the other. Mesh shows best-fit plane through the observed points, obtained by an ordinary least-squares fit giving equal weight to all points. Black line shows the best-fit linear combination of model-simulated anthropogenic and naturally forced temperature change. Length of pins shows residual climate variability (difference between observations and best-fit). Gradients of best-fit surface in anthropogenic and natural directions show best-fit scaling factors on CMIP5 ensemble mean anthropogenic and natural temperature change. For an animated visualisation of how this figure is constructed, please see the animation file provided as part of the Chapter 10 Supplementary Material. Uncertainty analysis of best-fit gradients in (c) using CMIP5 control variability.

**d).** Best-fit scaling factors on anthropogenic and natural temperature change, or gradients of the best-fit plane through observations from (c), shown by red diamond. Grey diamonds show corresponding gradients obtained applying an identical analysis to 114 non-overlapping 153-year segments (i.e., 17,442 years in total) of global mean surface temperature (GMST) from unforced control variability from the CMIP5 ensemble. For this heuristic example, control segments have not been masked as in the observations, but residuals are consistent with observed residual variability in both variance and power spectra. Black ellipse shows two-dimensional 90% confidence interval obtained by fitting an $F_{2,114}$ distribution to the grey diamonds. Red ellipse shows corresponding confidence interval centered on the best-fit gradients through the observations. Corresponding one-dimensional confidence intervals on scaling on model anthropogenic and natural warming shown by the red cross. Upper axis shows corresponding attributable anthropogenic warming 1951–2010 obtained from a straight-line fit to the CMIP ensemble mean anthropogenic warming. Location of red diamond and error bar on this axis indicate best-estimate and uncertainty in attributable anthropogenic warming.

### Figure 10.1, Figure 10.2, Figure 10.3

The right panels of Figure 10.1 (Figures 10.1d, e, f) are taken from Figure 3a of Forster et al. (2013 ), except that data from Fgoals-S2 have been excluded, and that 3-year smoothing to the data has not been applied here.

Process and data to create the leftmost panels of Figure 10.1; Figures 10.2 and 10.3 are described below. These figures are adapted from Jones et al. (2013 ).

**Data**
All of the data used were provided as monthly Netcdf files, from the CMIP3 and CMIP5 archives, and Daithi Stone (providing data used in the AR4 figures that were not in the CMIP3 archive). CMIP3 20C3M experiments were extended to 2012 by using A1B scenario simulations. CMIP5 historical experiments were extended to 2012 by using historicalExt and rcp4.5 experiments.

**Regridding**
All data are re-gridded onto the HadCRUT4 spatial grid (5° × 5°) since HadCRUT4 generally has the most restricted spatial coverage of the data sets considered here. There is no infilling into grid boxes with no observations. The re-gridding is done by area averaging any part of the old grid that lies within the new grid to produce a new gridpoint value.

**Masking**
The data coverage is limited to where data exists in the equivalent month/gridpoint of HadCRUT4.

**Creation of Annual Means**
Anomalies are calculated for each month/gridpoint relative to the 1961–1990 average, where at least 50% of the data in the reference period are needed to calculate the average. Annual means are calculated from monthly data for each calendar year, where at least 2 months are non-missing.

**Global Means**
GMST anomalies are calculated by area averaging all available gridpoint data for each year. For Figure 10.1 the average of the global mean for the reference period is calculated (1880–1919). The anomalies are then calculated with respect to the reference period.

### Figure 10.1

All model simulations are displayed even if they do not cover the whole period.

### Figure 10.2

For each gridpoint a linear regression is applied to the available data to calculate the trend, requiring no period longer than 5 consecutive years with missing data.

## Figure 10.3

For each latitude (on the HadCRUT4 grid), the average of the trend across the longitudes is calculated. Any of the observational data sets having less than 50% coverage of HadCRUT4's coverage at a given latitude are not shown on the figure at that latitude.

### Model Spread

For Figures 10.2 and 10.3 showing estimates of the spread of models, the 5 to 95% ranges are estimated by ordering the data (after weighting each simulation by the inverse of the number of simulations the model it belongs to has and multiplied by the number of models) and then choosing the central 90% range as limits (see Jones et al., 2013 ).

### Data

**Table 10.SM.1 |** Observational data sets.

| Observational Data Set | Period Covered |
|---|---|
| GISTEMP | 1880–2012 |
| HadCRUT4 | 1850–2012 |
| MLOST | 1880–2012 |

**Table 10.SM.2 |** Model Data. Summary of data used. Historical data were extended into the 21st century either by using any available A1B SRES simulations for CMIP3, and RCP4.5 for CMIP5, or RCP8.5 in cases where RCP4.5 was not available.

| | Archive | Number of models used (that cover 1901–2012 period) | Total number of members (that cover 1901–2012 period) |
|---|---|---|---|
| Historical | CMIP3 | 13 (9) | 63 (35) |
| | CMIP5 | 44 (40) | 147 (127) |
| historicalNat | CMIP3 | 6 (Hegerl et al., 2010) | 30 (Hegerl et al., 2010) |
| | CMIP5 | 17 (10) | 52 (38) |
| historicalGHG | CMIP3 | NA | NA |
| | CMIP5 | 16 (9) | 48 (35) |

## Figure 10.4

Scaling factors in (b) shown with a square are reproduced from Ribes and Terray (2013) (Figure 3, top right panel) and those in (d) are reproduced from Ribes and Terray (2013) (Figure 3, top left panel). In cases where Ribes and Terray (2013) show confidence ranges which include both plus and minus infinity, uncertainty bars are shown here as continuous across the range plotted. Scaling factors shown with a triangle in (b) are reproduced from Gillett et al. (2013 ) (Figure 4a), and those in (d) are reproduced from Gillett et al. (2013 ) (Figure S1). Results labelled 'multi' correspond to those labelled 'ObsU' in Gillett et al. (2013 ), and account for observational uncertainty and model uncertainty. Scaling factors in (b) shown with a diamond are reproduced from Jones et al. (2013 ) (Figure 16a). Results labelled 'multi' correspond to those labelled 'Weighted avg' in Jones et al. (2013 ). Corresponding attributable trends over the 1951–2010 period are taken directly from Jones et al. (2003) (Figure 16b), and are derived from the Ribes and Terray (2013) and Gillett et al. (2013 ) regression coefficients by multiplying regression coefficients for each forcing by the corresponding least squares trend in GMST simulated in response to that forcing over the 1951–2010 period. FGOALS-g2 was excluded from this figure because it did not include the effects of volcanic aerosol in its historicalNat simulations.

## Figure 10.5

This figure shows the assessed ranges derived as described in Section 10.3.1.1.3. We derive assessed ranges for the attributable contribution of greenhouse gases (denoted GHG, green), other anthropogenic forcings (OA, orange) and natural forcings (NAT, blue) by taking the smallest ranges with a precision of one decimal place that span the 5 to 95% ranges of attributable trends for the 1951–2010 period from the Jones et al. (2013 ) weighed multi-model analysis and the Gillett et al. (2013 ) multi-model analysis considering observational uncertainty (Figure 10.4a). The assessed range for the attributable contribution of combined anthropogenic forcings was derived in the same way from the Gillett et al. (2013 ) multi-model attributable trend shown in Figure 10.4c. The assessment of the internal variability is taken from the estimates of the 5th to 95th percentiles of 60-year trends of internal variability estimated by Knutson et al. (2013). We moderate our likelihood assessment and report likely ranges rather than very likely ranges directly implied by these studies in order to account for residual sources of uncertainty (see Section 10.3.1.1.3). Shown on the figure are the likely ranges shown as the whiskers with the end of the coloured bars being at the mid point of the attributable trend ranges. The midpoint of NAT is zero but the blue NAT bar is widened to make it visible.

## Figure 10.6

This figure is updated from the figure in Imbers et al. (2013) which is described in detail there. Estimates of contributions to global temperature changes are described in individual contributing papers.

Figure 10.6 is an updated version of an equivalent figure published in Imbers et al. (2013). The four studies represented in Figure 10.6 are identical to Figure 1 in Imbers et al. (2013); only the data from the Folland et al. (2013) have been updated. The four studies' aims were slightly different, as well as the signals included into the global mean temperature decomposition and length and sampling intervals of their time series. In what follows we briefly describe each of the studies represented in Figure 10.6.

The first study shown in Figure 10.6 is from Folland et al. (2013 ). Part of their aim was to forecast annual global mean temperature anomalies using a statistical model that estimates the contributions of six physical factors to GMST change and variability. The factors are net forcing from anthropogenic GHGs and aerosols, forcings from volcanic aerosols and changes in solar output, and the influences two internal modes of variability: El Niño-Southern Oscillation (ENSO) (represented by the first high-frequency eigenvector of global sea surface temperatures) and the Atlantic Multi-decadal Oscillation (AMO) (derived from the third low-frequency eigenvector of global sea surface temperatures of Parker et al. (2007)).

In their predictability analysis, the influence of these factors on observed surface temperatures is estimated from cross validated multiple linear regression using annual surface temperature values from 1891 to 2011 from an average of HadCRUT3, National Climate Data Centre (NCDC) and Goddard Institute of Space Studies (GISS). Owing to the cross validation method, an ensemble of 121 reconstructions of the observed variable is obtained. In our analysis we show the ensemble mean time series and its 95% confidence range resulting from regression with the HadCRUT3 data set alone to 2012, giving 122 reconstructions. There are two differences between the way the ENSO and volcanic predictors are used here and in Folland et al. (2013). In Figure 10.6 appropriately smoothed volcanic and solar data simulated to the end of each year are used as well as ENSO data simulated from January to September of each year. In Folland et al. (2013) the ENSO data used for the prediction of a year were averaged over October and November of the previous year while the volcanic and solar data used were simulated up to the end of the previous year. Imbers et al. (2013) used an earlier version of the data of Folland et al. (2013) with the same differences in the way ENSO and volcanic predictors are used but using annual surface temperature values from 1891 to 2010 from an average of HadCRUT3 as training data for the statistical model, updated here using annual surface temperature values from 1891 to 2012.

Lean and Rind's (2009) results are also shown in Figure 10.6. Their goal was to forecast global and regional climate change in the near future by decomposing the observed record of monthly mean surface air temperature in terms of its combined linear response to ENSO, solar and volcanic activity and anthropogenic influences (Lean and Rind, 2008; see also Kopp and Lean, 2011). They used 1980–2008 monthly time series of mean surface temperature anomalies with respect to 1951–1980 and performed a multivariate linear regression against the instrumental surface temperature record HadCRUT3v (Brohan et al., 2006) to find the optimal combination of those four signals that better explain that record. Their solar, volcanic, anthropogenic and ENSO signals are lagged by 1, 7, 120 and 4 months respectively with respect to the temperature observations in order to maximize the proportion of global variability that the statistical model captures (76% of the variance observed since 1980).

The results of the third study considered in Figure 10.6 are from Kaufmann et al. (2011), who used a statistical model derived to estimate the relation between emissions of carbon dioxide ($CO_2$) and methane ($CH_4$), the concentrations of these gases, and global surface temperature (Kaufmann et al., 2006), to evaluate whether anthropogenic emissions of radiative active gases along with variability can account for the 1998–2008 hiatus in warming. The model is estimated with annual data from 1960 to 1998 and used to project 1998–2008 temperatures. The signals included in this model are: GHGs, anthropogenic sulphur emissions, solar insolation, ENSO (represented by the Southern Oscillation Index (SOI)) and radiative forcing of volcanic sulphates.

The last study shown in Figure 10.6 is from Lockwood (2008). Lockwood (2008) intended to analyse the contribution of changes in solar output to global mean surface temperature. The statistical model consists on a multivariate fit to the global monthly mean surface temperature anomaly for the period 1953–2007. The signals included in the fit are the solar, volcanic and anthropogenic components (the latest as a linear trend), and the ENSO3.4 index to represent the effect of El Niño.

## Figure 10.7

Taken from Figure 7 of Jones et al. (2013 ).

## Figure 10.8

The figure is adapted from Lott et al. (2013).

### Observational Data Sets

A number of new radiosonde data sets have been developed since the studies of a decade ago. Following the review by Thorne et al. (2011) and having assessed which sets had coverage for the entire period, four data sets were chosen for analysis. The first of these is Hadley Centre Atmospheric Temperature data set 2 (HadAT2) (Thorne et al., 2005). Of the observational data sets, this has the least spatial coverage, and thus is used as a common mask for all other data, both observations and models, to allow a like-for-like comparison.

The other three observational data sets are from the Radiosonde Innovation Composite Homogenization RAdiosone OBservation COrrection using REanalyses (RICH/RAOBCORE) family (Haimberger et al., 2012). The first of these sets used is RAOBCORE 1.5, which uses the European Centre for Medium Range Weather Forecasts (ECMRWF) 40-year reanalysis (ERA-40) (Uppala et al., 2005) and ERA-Interim reanalyses (Dee et al., 2011) to detect and adjust breakpoints. The other two are the ensembles of realizations known as RICH-obs 1.5 and RICH-$\tau$ 1.5. Both of these generate the ensemble by varying processing decisions (such as minimum number of data points or treatment of transitions), with breakpoint detection derived from RAOBCORE. However, they differ in the way they handle the adjustments. RICH-obs makes adjustments by directly comparing station time series, while RICH-$\tau$ compares the differences between the time series and the ERA-Interim background.

### Model Data Sets

For the selection of model data sets, the decision was limited by the need for that model to have runs with natural forcings (NAT), as well as runs with only GHG forcings and finally with all historical (i.e., anthropogenic and natural) forcings (ALL), between 1961 and 2010 available on the CMIP5 (Taylor et al., 2012) archive at the time the analysis was undertaken. This led to the models shown in Table 10.SM.3 being used.

**Table 10.SM.3 |** CMIP5 models used for this study, and the number runs with each forcing.

| Modelling Centre (or Group) | Model(s) | Members Included | | |
|---|---|---|---|---|
| | | ALL | NAT | GHG |
| Commonwealth Scientific and Industrial Research Organization in collaboration with Queensland Climate Change Centre of Excellence | CSIRO-Mk3.6.0 | 10 | 5 | 5 |
| NASA Goddard Institute for Space Studies | GISS-E2-R | 5 | 5 | 5 |
| | GISS-E2-H | 5 | 5 | 5 |
| Canadian Centre for Climate Modelling and Analysis | CanESM2 | 5 | 5 | 5 |
| Met Office Hadley Centre | HadGEM2-ES | 4 | 4 | 4 |
| Beijing Climate Center, China Meteorological Administration | BCC-CSM1.1 | 3 | 1 | 1 |

All data sets were adjusted to a common temperature anomaly relative to the 1961–1990 climatology, re-gridded to the HadAT2 grid and masked before zonal averages were taken. The following set of pressure levels common to all data sets was used: 850, 700, 500, 300, 200, 150, 100, 50 and 30 hPa. The three latitude bands analyzed are a tropical zone (20°S to 20°N) and north and south extratropical zones (60°S to 20°S and 20°N to 60°N), along with the average over the whole studied area (i.e., 60°S to 60°N).

Different from Lott et al. (2013) Figures 10.8 and 10.SM.1 do not include the Centre National de Recherches Météorologiques (CNRM-CM5) and Norwegian Earth System Model 1-M (NorESM1-M) models. CNRM-CM5 was excluded because of unrealistic stratospheric ozone forcing (Eyring et al., 2013). The NorESMI-M was not included because the GHG single forcing runs for this model also include ozone forcing.

### Trend Calculations

For both the models and observations, the trends at each pressure level were calculated using a median pairwise algorithm (as this copes better with outliers than a conventional linear fit) (Lanzante, 1996). These trends were plotted against pressure level, for all models and forcings within them. For each forcing ensemble of model runs, the shaded region shows the 5 to 95% range determined based on individual runs. Red represents all-forcings runs, blue shows natural forcings and green is GHG-forced only. The thick black line is HadAT2, thin black line is RAOBCORE 1.5, while the dark grey band is the RICH-obs 1.5 ensemble range and light grey is the RICH-$\tau$ 1.5 ensemble range. Each band is displayed 25% translucent to better distinguish where forcings and observations overlap.

Trend caluclation shown in Figure 10.8 are for the period 1961–2010. Figure 10.SM.1 shows trend calcuations for the satellite period from 1979 to 2010.

## Figure 10.9

This figure shows time series of annual mean lower stratosphere temperatures from three satellite data sets and CMIP5 experiments. It utilizes the same CMIP5 model runs as Figure 10. 8 and individual model runs are shown. Synthetic lower stratosphere temperatures were calculated using global Microwave Sounding Unit (MSU) vertical weighting functions for the lower stratosphere. The three observational data sets are used to address observational consistent: Remote Sensing System (RSS) Version 3.3, University of Alabama in Huntsville (UAH) version 5.4 and Situation, Task, Action, Result (STAR) version 2.0 (Santer et al., 2013).

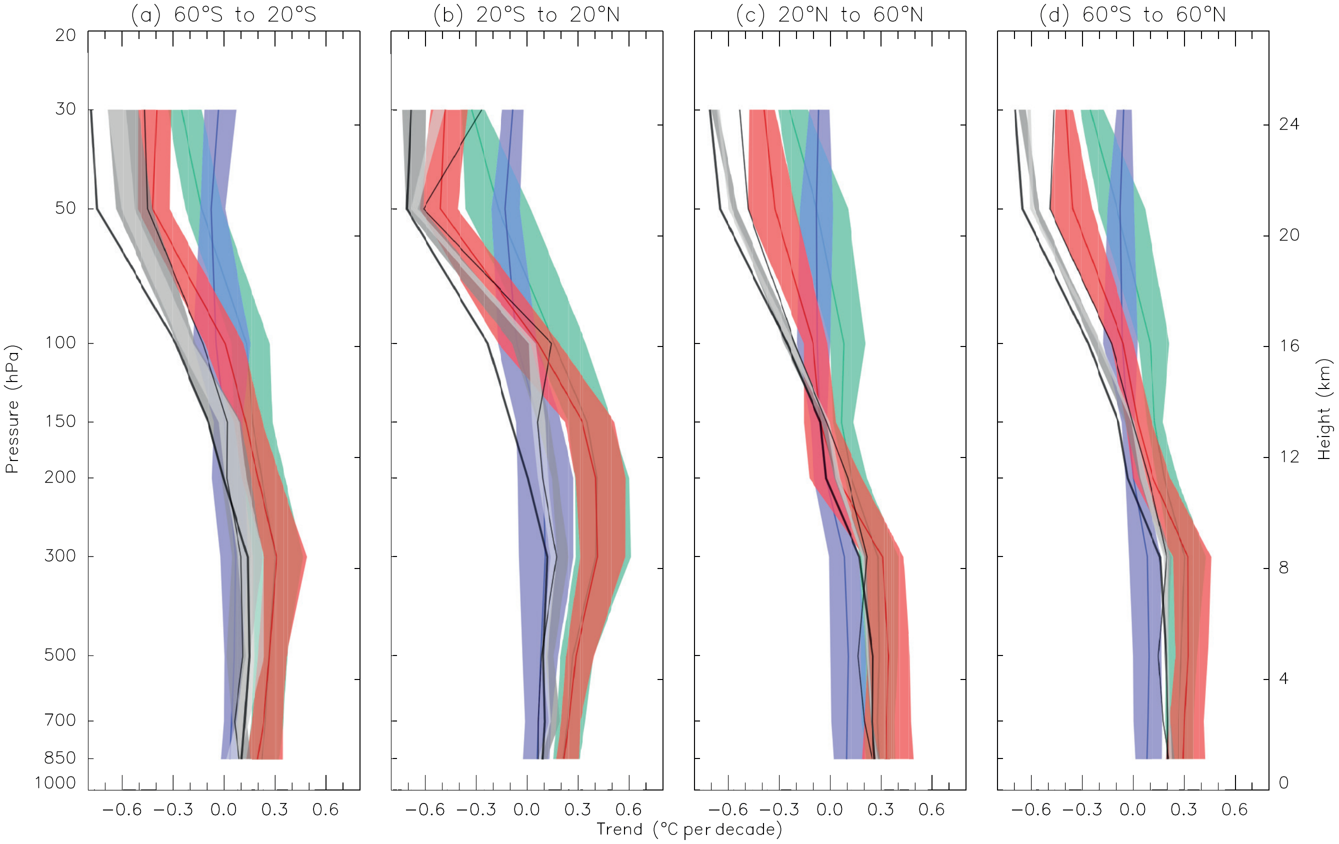

**Figure 10.SM.1 |** Observed and simulated zonal mean temperatures trends from 1979 to 2010 for CMIP5 simulations containing both anthropogenic and natural forcings (red), natural forcings only (blue) and greenhouse gas forcing only (green) where the 5th to 95th percentile ranges of the ensembles are shown. Three radiosonde observations are shown (thick black line: Hadley Centre Atmospheric Temperature data set 2 (HadAT2), thin black line: RAdiosone OBservation COrrection using REanalyses (RAOBCORE) 1.5, dark grey band: Radiosonde Innovation Composite Homogenization (RICH)-obs 1.5 ensemble and light grey: RICH- $\tau$ 1.5 ensemble. (Adapted from Lott et al. (2013) but for the more recent period from 1979 to 2010.)

Synthetic MSU temperature time series from model data were calculated as follows:

1. Select area from 82.5°S to 82.5°N of atmosphere temperature fields and time period and calculate area weighted averages.

2. Select time series from January 1979 to December 2010 and calculate annual averages and anomalies relative to the period 1996–2010.

3. Select pressure levels (hPa): 1000, 925, 850, 700, 600, 500, 400, 300, 250, 200, 150, 100, 70, 50, 30, 20, 10.

4. Apply vertical weighting function for MSU lower stratosphere temperature (channel 4) (Mears and Wentz, 2009).

## Figure 10.10

Figure 10.10 is updated from Supplementary Information Figure S1 of Balan Sarojini et al. (2012 ). The updates include the use of a 11-year smoothing rather than a 5-year smoothing used in Balan Sarojini et al. (2012 ) and simulations from additional models for ALL that have become available since the publication of the paper and that are listed below.

Global and zonal average changes in annual mean precipitation (in mm day$^{-1}$) for the period 1951–2005, with regard to the baseline period of 1961–1990, are plotted based on Balan Sarojini et al. (2012 ).

CMIP5 Simulations used are:
**Historical ('All'):** HadGEM2-ES, CSIRO-Mk3-6-0, CNRM-CM5, NorESM1-M, CanESM2, BCC-CSM1-1, INMCM4_ESM, IPSL-CM5A-LR, GISS-E2-H, GISS-E2-R, MPI-ESM-LR, GFDL-ESM2G, GFDL-ESM2M, CCSM4, MIROC5, MIROC-ESM, MIROC-ESM-CHEM, MRI-CGCM3, IPSL-CM5A-MR, CESM1-BGC, CESM1-CAM5, CESM1-WACCM, CESM1-FASTCHEM, ACCESS1-0, GFDL-CM3, CMCC-CMS, CMCC-CESM, HadGEM2-CC, NorESM1-ME, MPI-ESM-MR.

**HistoricalNat ('Nat'):** HadGEM2-ES, CSIRO-Mk3-6-0, CNRM-CM5, NorESM1-M, CanESM2, BCC-CSM1-1, MIROC-ESM, MIROC-ESM-CHEM, MRI-CGCM3, GFDL-CM3.

There are 30 'All' runs (one each of 30 CMIP5 models forced with both anthropogenic and natural forcings) and 10 'Nat' runs (one each of 10 CMIP5 models forced with natural forcings only)

Observation used is a gridded observational data set based on station data extracted from the Global Historical Climatology Network (updated from Zhang et al. (2007)). Monthly data for the period 1951–2005, quality controlled and gridded at 5° × 5°, for all land grid squares on the globe for which station data are available, are used. In order to avoid artefacts arising from changes in data coverage, a sampling criterion of choosing data available for >90% of the analysis period is applied (i.e., each spatial grid point is chosen when data over 90% of the years (only those years that have data for all months) are present).

### Masking of Simulated Data onto the Observational Grid

First, the land area of the simulated data available in different spatial resolutions is obtained by choosing a grid point as land when its land area fraction is greater than or equal to 70%. Second, the simulated land data are interpolated to the 5°× 5° observational grid using bilinear interpolation. Third, the 90% sampling criterion is applied to each regridded model data to obtain the consistent temporal and spatial data coverage for the simulated and observed data.

### Calculation of Spatial and Annual Averages and Anomalies with regard to the Baseline Climatology

For each (regridded and sampled) monthly model data, spatial averages are first calculated for the global domain and zonal bands of 60°N to 90°N, 30°N to 60°N and 30°S to 30°N. Annual averages, baseline climatology (for 1961–1990) and anomalies from the baseline period are then calculated.

### Calculation of Multi-model Means of 'All' and 'Nat' Runs

Multi-model averages of 30 All runs and 10 Nat runs are calculated.

### Decadal Smoothing for both Observed and Simulated Data

A smoothing of boxcar average with 11-year width (with edges truncated) is applied to the resulting time series of annual precipitation anomalies.

### Plotting

The yearly anomalies are plotted with a *y*-axis range of 1950–2010. Multi-model means are in thick solid lines (All in red and Nat in blue) and individual simulations are in thin solid lines.

### Statistical Test of Significance for the Changes Between 'All' and 'Nat' Runs

Green stars are plotted when the changes are statistically significant at 5% level ($p < 0.05$) between the ensemble of runs with both anthropogenic and natural forcings (red lines) and the ensemble of runs with just natural forcings (blue lines) using a two-sample two-tailed *t*-test for the last 30 years of the time series.

## Supplementary Figure to Figure 10.10: Figure 10.SM.2

Global and zonal average changes in annual mean precipitation (in mm day$^{-1}$) for the period 1951–2005, with regard to the baseline period of 1961–1990, are plotted.

The details of the simulations and procedure for both simulations and observations are same as that for Figure 10.10 except for the observational data set used and an additional sampling criterion as described below (i.e., Steps 2 and 3).

Observation used is a gridded observational dataset based on station data extracted from the Climatic Research Unit (updated from CRU TS3.1 of Harris et al. (2013) and sampled as in Polson et al. (2013)). Monthly data for the period 1951–2005, quality controlled and gridded at 0.5° × 0.5°, are used.

This data is first interpolated to the common spatial resolution (as to Figure 10.10) of 5°× 5°. In order to avoid artefacts arising from changes in data coverage, two sampling criteria are applied: (1) station sampling criterion (Polson et al., 2013) of choosing only those 5° × 5° grid boxes that have at least one station (in any 0.5° × 0.5° grid box) for the coastal grid boxes and with at least two stations for the inland grid boxes. A 5° × 5° grid box is coastal when more than half of number of the 0.5° × 0.5° boxes is ocean points. (2) A criterion of choosing data available for >95% of the analysis period is applied, that is, each spatial grid point is chosen when data over 95% of the years (years that have data available for any number of months) are present.

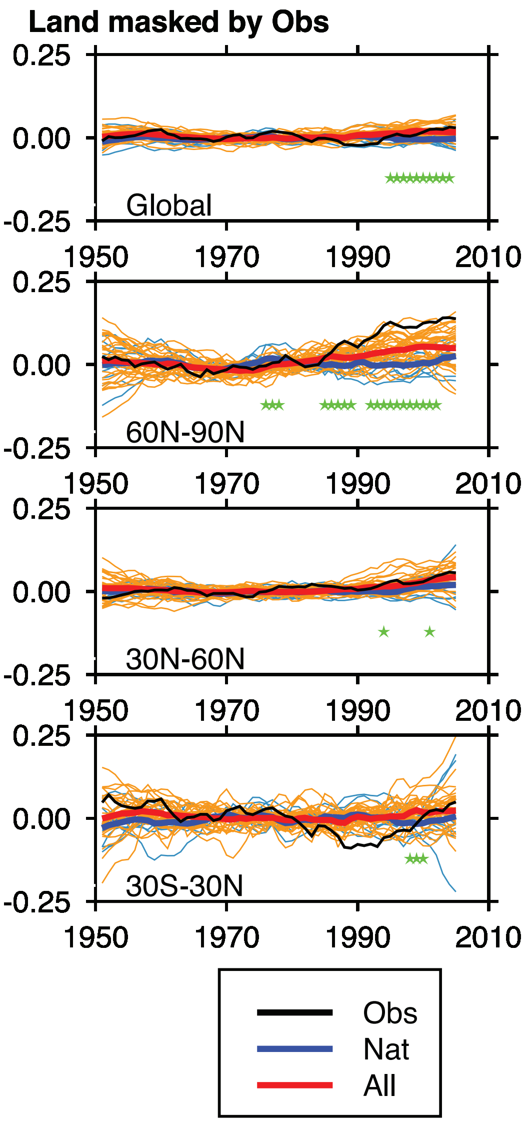

**Figure 10.SM.2 |** Global and zonal average changes in annual mean precipitation ($\text{mm day}^{-1}$) over areas of land where there are observations, expressed relative to the baseline period of 1961–1990, simulated by CMIP5 models forced with both anthropogenic and natural forcings (red lines) and natural forcings only (blue lines) for the global mean and for three latitude bands. Multi-model means are shown in thick solid lines. Observations (gridded values derived from Climatic Research Unit (CRU) station data, updated from CRU TS3.1 of Harris et al. (2013) and sampled as in Polson et al. (2013) are shown as a black solid line. An 11-year smoothing is applied to both simulations and observations. Green stars show statistically significant changes at 5% level ($p < 0.05$) between the ensemble of runs with both anthropogenic and natural forcings (red lines) and the ensemble of runs with just natural forcings (blue lines) using a two-sample two-tailed $t$-test for the last 30 years of the time series.

### Masking of Simulated Data onto the Observational Grid

First, the land area of the simulated data available in different spatial resolutions is obtained by choosing a grid point as land when its land area fraction is greater than or equal to 70%. Second, the simulated land data are interpolated to the 5° × 5° observational grid using bilinear interpolation. Third, the mask of station sampling and the 95% sampling (described in Step 2) is applied to each regridded model data to obtain the consistent temporal and spatial data coverage for the simulated and observed data.

## Figure 10.11

Figure based on Zhang et al. (2007); Min et al. (2008); Min et al. (2011); Polson et al. (2013).

Left top panel: (a) Global land-annual results from Zhang et al. (2007) (first pair of bars) and Polson et al. (2013) (2nd to 5th pair of bars); (b) global land-seasonal results from Polson et al. (2013); (c) Arctic results from Min et al. (2008) and (d) extreme results from Min et al. (2011). Right top panel: After Zhang et al. (2007), but updated following Polson et al. (2013): changes expressed in percent climatology and CMIP5 models plotted. Bottom left and right panel: from Polson et al. (2013).

## Figure 10.12

December to February mean change of southern border of the Hadley circulation. Unit is degree in latitude per decade. Reanalysis data sets are marked with different colours. Trends are all calculated over the period of 1979–2005. According to CMIP5, historicalNAT, historicalGHG and historical denote historical simulations with natural forcing, observed increasing GHG forcing and all forcings, respectively. For each reanalysis dataset, the error bars indicate the 95% confidence level of the standard $t$-test. For CMIP5 simulations, trends are first calculated for each model, and all ensemble members are used. Then, trends are averaged for multi-model ensembles. Trend uncertainty is estimated from multi-model ensembles, as twice the standard error. This figure is adapted from Hu et al. (2013) with additional trends derived from Climate Forecast System Reanalysis (CSFR) and Modern Era Retrospective-analysis for Research and Applications (MERRA) reanalyses.

## Figure 10.13

Figure 10.13 is adapted from Gillett and Fyfe (2013) (Figure S4), with the following changes. Simulations from the following numbers of models which cover the 1951–2011 period were used: 106 historical simulations from 34 models, 26 historicalGHG simulations from 7 models, 11 aerosols-only simulations from 3 models, 15 ozone-only simulations from 3 models, and 48 historicalNat simulations from 10 models, and control simulations from 43 models. As well as the 5 to 95% range of trends simulated in the historical simulations (red boxes), the 5 to 95% ranges of trends simulated in the control simulations (grey bars) are also shown. These ranges were derived by weighting each simulation by the inverse of the product of the number of models and the number of simulations from the model concerned, ranking the trends, deriving a cumulative distribution function by summing the weights, and then interpolating to find the 5th and 95th percentiles, following Jones et al. (2013 ). Mean responses to each forcing were derived by first averaging ensemble members for each model, and then averaging across models. Uncertainty bars shown for individual forcings are uncertainties in the mean response to each forcing, calculated by dividing the standard deviation across models by the square root of the number of models, and multiplying by the Student-*t* statistic for a cutoff value of 0.05 and with the number of degrees of freedom equal to one less than the number of models. A minor error effecting Gillett and Fyfe (2013) Figure S4 only in which the northern reference latitude for the Southern Annular Mode (SAM) index was 45°S instead of 40°S following Gong and Wang (1999) was corrected.

## Figure 10.14

### Panel (a)

This figure is an update of Figure 2 of Domingues et al. (2008). In this figure:

CMIP5 simulations are:
**HistoricalNat** (can_esm2, ccsm4, cnrm_cm5, csiro_mk3.6, giss_e2_h, giss_e2_r, hadgem2-es, miroc_esm, mri_cgcm3, nor_esm1_m)

**Historical** (can_esm2, ccsm4, cnrm_cm5, csiro_mk3.6, giss_e2_h, giss_e2_r, hadgem2-es, miroc5, miroc4h, miroc_esm, mpi_esm_lr, mri_cgcm3, nor_esm1_m)

Annual mean ocean heat content (OHC) values are calculated from models by vertically integrating the annual mean temperature anomalies (with respect to a 1960–1980 reference period). Global mean time series are calculated by integrating over space.

Observed global OHC changes from Domingues et al. (2008); also with a reference period of 1960–1980) are smoothed (three-year running means) and plotted.

Stratospheric Aerosol loading (as global mean AOD) from Sato et al. (1993); data downloaded from the website http://data.giss.nasa.gov/modelforce/strataer/#References before their December 2012 update) is plotted. A three-year running mean is also calculated and plotted for comparison against smoothed data.

### Panel (b)

This figure is based on Figure 5(c) of Gleckler et al. (2012).

Anomalies of volume average temperature $\Delta T$ rather than ocean heat content are used.

Observed $\Delta T$ estimates are based on globally gridded (1° × 1° latitude/longitude) products, not raw measurements. The observed datasets used are:

> Pre-XBT bias correction data: Levitus et al. (2005) and Ishii et al. (2006)
>
> XBT bias corrected data: Levitus et al. (2009), Ishii and Kimoto (2009) and Domingues et al. (2008)

Annual means of all model ocean temperature data 700 m of the ocean column have been interpolated to the spatial grid and standard vertical depth levels of the observational data (Ishii and Kimoto, 2009).

From the CMIP3, control and 20th century (20CEN) runs are considered. The models are further classified as:

> VOL models (those that included volcanic and other natural forcings) are CCSM3.0, GFDL-CM2.0, GISS-EH, GISS-ER, MIROC-CG-CM2.3.2, MRI-CGCM2.3.2
>
> NoV models are those that did not include natural forcings. These are CCCma-CGCM3.1, CNRM-CM3, CSIRO-Mk3.0, GISS-AOM, FGOALS-g1.0 and UKMO-HadCM3.

The observed and model simulated historical anomalies are calculated with respect to a 1957–1990 climatology and all control-run anomalies are with respect to the overall time mean of each model's control run.

Each 20CEN simulation is subsampled in the same manner using the 1960–1999 (Ishii, 2009).

Basin-scale $\Delta T$ changes in the North Atlantic, South Atlantic, North Pacific, South Pacific, North Indian, and South Indian oceans are computed.

Residual drift associated with the incomplete spin-up of model control runs is removed from all $\Delta T$ basin-average time series using a quadratic fit. Quadratic fits are computed for the entire control, yielding a drift estimate. This drift is then removed from the original control, yielding an estimate of the true model noise. For each 20CEN simulation, there is a contemporaneous section of the corresponding control and a contemporaneous section of the control-drift estimate. This section of the control drift is removed from the 20CEN simulation.

The $\Delta T$ anomalies of each ocean basin are then weighted by its volume.

CMIP3 20CEN runs (1870–1999) are averaged together to produce a Multi-Model Response (MMR). If more than one realization of the 20CEN experiment is available for an individual model, these realizations are averaged together before averaging across models.

The fingerprint is the first Empirical Orthogonal Function (EOF) of the MMR of $\Delta T$ in the six ocean basins, calculated over 1960–1999. Fingerprints are computed separately for the simulations that include volcanic (V) or exclude volcanic eruptions (NoV) MMRs.

The multimodel noise estimates are based on concatenating all available control data from VOL models.

The basin-average upper-ocean temperature changes from observations are projected onto the fingerprint yielding the signal projection time series $Z(t)$.

Trends of increasing length $L$ (least squares fit starting from 1970 and with an initial $L$ of 10 years) are fit to this time series to yield the "signal".

Similarly, the $\Delta T$ from the VOL concatenated control runs are projected onto the searched-for fingerprint. The resulting projection time series, $N(t)$, provides information about unforced changes in pattern similarity.

$L$-year, non-overlapping trends are fitted to $N(t)$, with $L$ varying from 10, 11, 12,…39 years. For a given value of $L$, the noise is the standard deviation of the sampling distribution of the trends.

With these, the signal-to-noise (S/N) ratio is calculated as a function of $L$. The detection time is defined as the year at which S/N ratio exceeds and remains above a stipulated 5% significance threshold.

## Figure 10.15

This figure is from three published studies. Panel A is adapted from Figure 3 of Helm et al. (2010). The top and bottom panels of Figure 3 are shown in Panel A of Figure 10.15. Panel B is redrafted and simplified from the original figure, Figure 2A of Durack et al. (2012). Panel C is taken from Figure 11a from Terray et al. (2012).

## Figure 10.16

Figure 10.16: September sea ice extent for Arctic (top panel) and Antarctic (bottom panel) adapted from Wang and Overland (2012). Only CMIP5 models which simulated seasonal mean and magnitude of seasonal cycle in reasonable agreement with observations are included in the plot.

The grey lines are the runs from the pre-industrial control simulations, and the red lines are from Historical simulations patched with RCP8.5 runs for the period 2005–2012. The black line is based on the sea ice extent data are from National Snow and Ice Data Center (NSIDC).

There are 24 ensemble members from 11 models for the Arctic and 21 members from 6 models for the Antarctic plot.

The list of simulations that passed the acceptance criteria and plotted in the figure is:
**Northern Hemisphere:** ACCESS1.0, ACCESS1.3, CCSM4, CESM1-CAM5, EC-EARTH, HadGEM2AO, HadGEM2CC, HadGEM2ES, MIROC-ESM, MIROC-ESM-C, MPI-ESM-LR.

**Southern Hemisphere:** ACCESS1.3, CMCC-CM, CanESM2, EC-EARTH, MRI-CGCM3, NorESM1-M.

The underlined models are those identified and used by Wang and Overland (2012).

The criteria for choosing acceptable simulations models is as follows. The simulated mean and seasonal cycle of the sea ice extent is within 20% of the observations of the sea ice climatology for the 1981–2005 period. The 1981–2005 period was chosen because it overlaps with satellite observation period and 2005 is the last year of the historical simulations. The 20% bound chosen here is used in Wang and Overland (2012), and has also been used by Zhang (2010). A total of 36 models were evaluated against these selection criteria.

## Figure 10.17

Figure 10.17: Zwiers et al. (2011).

Figure 10.17: Detection results for changes in intensity and frequency of extreme events. Right-hand sides of each panel show scaling factors and their 90% confidence intervals for changes in the frequency of temperature extremes for winter (October to March for Northern Hemisphere and April to September for Southern Hemisphere), and summer half years. TN10, TX10 are respectively the frequency for daily minimum and daily maximum temperatures falling below their 10th percentiles for the base period 1961–1990. TN90 and TX90 are the frequency of the occurrence of daily minimum and daily maximum temperatures above their respective 90th percentiles calculated for the 1961–1990 base period (Morak et al., 2013), fingerprints are based on simulations of Hadley Centre new Global Environmental Model 1 (HadGEM1) with both anthropogenic and natural forcings). Left side of each panel show scaling factors and their 90% confidence intervals for intensity of annual extreme temperatures in response to external forcings for the period 1951–2000. TNn and TXn represent annual minimum daily minimum and maximum temperatures, respectively, while TNx and TXx represent annual maximum daily minimum and maximum temperatures. This is updated from Zwiers et al. (2011) by conducting exactly the same type of analysis of Zwiers et al. (2011) using spatial domain defined in Morak et al. (2013), fingerprints are based on simulations of climate models with both anthropogenic and natural forcings). Detection is claimed at the 10% significance level if the 90% confidence interval of a scaling factor is above zero line.

## Figure 10.18

Figure 10.18 combines three figures which are adapted from three different papers to provide an overview of different results for attribution studies using changes in return time as a measure for anthropogenic influence.

Figure 10.18a is directly taken from Pall et al. (2011). The figure is identical to Figure 3d in the paper.

Figure 10.18b is adapted from Kay et al. (2011). The first row of Figure 5 in the paper shows the return times of 1-day flood peaks in the catchment area 27007 (river Ure, UK) for the period October 2000 to March 2001 comparing simulations with actual year 2000 climate drivers to four (Figure 5 a–d) different sets of counterfactual year 2000 climate drivers. The counterfactual ensembles represent four possible sets of surface temperatures (SSTs) representative of a 'world that might have been' without anthropogenic climate forcing. Different SST patterns are obtained from four different models (columns a–d) with different scaling factors for the SSTs (colours). We adapted this figure as follows. Instead of calculating the 6-month period October 2000 to March 2001 we considered only the period January 2001 to March 2001 to assess changes in the return time of 1-day peak floods in spring. In addition, the catchment used for this study is not the river Ure but the river Don in South Yorkshire, UK. Furthermore we combined the different SST patterns from all models in one figure.

Figure 10.18c is directly taken from Otto et al. (2012). The figure is identical to Figure 4 in the paper but without displaying temperature equivalents for ERA-interim reanalysis data.

## Figure 10.19

All reconstructions used are the same as in Schurer et al. (2013), with the exception of the Mann et al. (2009) reconstruction, which in the top panel is for 30°N to 90°N land and sea and in the bottom panel is for 0° to 60°E 25°N to 65°N land and sea and the Luterbacher et al. (2004) reconstruction which is for the region 25°W to 40°E 35°N to 70°N land only (bottom panel).

All models used to construct the multi-model ensemble and the control simulations used for samples of internal variability are the same as in Schurer et al. (2013) (see Table 10.SM.4). To calculate the multi-model mean each model set-up contributes equally, that is, the mean of the five Max Planck Institute Community Earth Systems Models (MPI-COSMOS) simulations counts as one model whereas the GISS-E2-R simulations are treated separately because they contain different forcings. The GISS-E2-R simulations included a significant initial model drift which was removed from the control simulation by fitting a second order polynomial to the control simulation. The bold orange line in the figure shows the noise reduced multi-model mean multiplied by the best-fit scaling factor. The uncertainty range is calculated by adding in quadrature the uncertainty in the scaling range to the uncertainty due to internal variability.

The Goosse simulations are taken directly from the simulation described in Goosse et al. (2012a, 2012b), constrained by the Mann et al. (2009) reconstruction from 30°N to 90°N.

In the top panel the annual mean of the region 30°N to 90°N land and sea is shown and in the bottom panel the annual mean of the region 0° to 60°E, 25°N to 65°N. The uncertainty range was estimated from the uncertainty given in Goosse et al. (2012a) and Goosse et al. (2012b) for the annual data-assimilated results. To account for the smoothing used in the figure these calculated annual standard deviations were scaled by the ratio between the standard deviation of the smoothed and un-smoothed control runs used in Schurer et al. (2013).

The instrumental data is taken from Morice et al. (2012).

All analysis is done on decadally smoothed time-series, using first a 10-year Butterworth filter and then an 11-year box car filter. The analysis shown in the bottom panel uses the same method and model data as used for the top panel, but is performed on the European domain, following Hegerl et al. (2011).

## Figure 10.20a

The plot contains three different types of reporting on transient climate response (TCR) estimation studies: (A) bars indicating estimates of the range of possible TCR values (most, but not all, are 5 to 95% confidence interval estimates), (B) these studies are included with both, a confidence range represented by a bar and a corresponding probability density function (PDF), and (C) some studies from AR4 are included just with their PDFs to show the contrast between AR4 and AR5.

### Bar-Plot (without Probability Density Functions)

Schwartz (2012) uses a two-time scale formulation of the climate system response (e.g., see Gregory, 2000; Held et al., 2010) to obtain TCR estimates (more specifically using the notion of transient climate sensitivity, more generally defined without reference to a specific rate of increase in concentration) ranging from 0.9°C to 1.9°C, the lower values corresponding to higher values of net forcing over the 20th century. The range in the figure is generated by multiplying the headline values from the paper (0.23 ± 0.01 to 0.51 ± 0.04) K (W $m^{-2}$)$^{-1}$, with an assumed forcing for a doubling of $CO_2$ of 3.7 W $m^{-2}$ (leading to (0.85 to 1.89 K)). The given range originates from an ensemble of different published forcing estimates, and hence it cannot directly be interpreted as a 5 to 95% confidence interval.

Libardoni and Forest (2011) show that the TCR along with other climate system parameters (see below) can be estimated by comparing EMIC simulations with a range of 20th century surface temperature atmospheric and ocean temperature data sets. Under a variety of assumptions, they obtain 5 to 95% ranges for TCR spanning 0.9 to 2.4 K. These values are directly taken from the 2011 paper (0.87 to 2.41 K). Updating this study to include data to 2004 gives results that are essentially unchanged.

**Table 10.SM.4 |** Details of the models used.

| Model | Ensemble Members | Resolution | | Forcings | | | |
|---|---|---|---|---|---|---|---|
| | | Atmosphere | Ocean | Volcanic | Solar | Greenhouse Gas | Land Use |
| CCSM4* | 1 | 288 × 192 × L26 | 320 × 384 × L60 | GRA | VK/WLS | SJA | PEA/Hur |
| MPI-COSMOS | 5 | 96 × 48 × L19 | GR3.0 × L40 | CEA | JLT | Interactive | PEA |
| MPI-ESM-P* | 1 | 196 × 98 × L47 | 256 × 220 × L40 | CEA | VK/WLS | SJA | PEA |
| HadCM3 | 1 | 96 × 73 × L19 | 288 × 144 × L20 | CEA | SBF/WLS | SJA | PEA |
| GISS-E2-R* | 1 | 144 × 90 × L40 | 288 × 180 × L32 | CEA | VK/WLS | SJA | PEA/Hur |
| GISS-E2-R* | 1 | 144 × 90 × L40 | 288 × 180 × L32 | GRA | VK/WLS | SJA | KK11/Hur |
| Bcc-csm1-1* | 1 | 128 × 64 × L40 | 360 × 232 × L40 | GRA | VK/WLS | SJA | X |

Notes:

Further details can be found in the references for the model and the forcings used; the references for the models are: CCSM4 – Landrum et al. (2013); MPI-COSMOS – Jungclaus et al. (2010); HadCM3 – Schurer et al. (2013); Bcc-csm1-1 – Wu (2012). The references for the forcings are: CEA –Crowley et al. (2008), GRA –Gao et al. (2008), VSK –Vieira et al. (2011), SBF –Steinhilber et al. (2009) , WLS –Wang et al. (2005), SJA –Schmidt et al. (2012), PEA –Pongratz et al. (2008), Hur- Hurtt et al. (2009), KK11 –Kaplan et al. (2009), JLT –Jungclaus et al. (2010), MM - MacFarling Meure et al. (2006). An X indicates that the forcing is not included. The models indicated by asterisks have been made available as part of the CMIP5 project.

Padilla et al. (2011) use a simple two-time scale model (see the entry on Schwartz above) to derive an observationally constrained estimate of the TCR of 1.3°C to 2.6°C. The range is directly taken from the headline results of the cited paper, with a best estimate of 1.6 K, and including an estimate how the 90% confidence range will change in the future (reduction of 45% by 2030).

Gregory and Forster (2008) estimate real world TCR as 1.3 to 2.3 K (5 to 95% uncertainty range) from the data of 1970–2006, assuming a linear relationship between radiative forcing and GMST change and disregarding any trend caused by natural forcing. The numbers are directly taken from the cited paper (abstract).

Stott and Forest (2007) used the observed 20th century temperature change to constrain three models (HadCM3, GFDL-R30 and PCM) and then applied these models to the calculation of TCR for the future. The calculated TCR is around 2.1 K and the 5 to 95% probability range is 1.5 to 2.8 K. The numbers are directly taken from the description of Figure 8 of the cited paper.

Gillett et al. (2013 ) base their methodology on Gillett et al. (2012) and Stott and Jones (2012), but including a broader range of model and observational uncertainties, in particular addressing the efficacy of non-$CO_2$ gases, and find a TCR range of 0.9°C to 2.3°C. This confidence range is directly taken from Figure 7a of the cited paper.

Tung et al. (2008) examined the response to the 11-year solar cycle using discriminant analysis, and found a high range for TCR: >2.5°C to 3.6°C. These numbers are directly taken from Equation 7 of the cited paper. However, this estimate may be affected by different mechanisms by which solar forcing affects climate and possible aliasing with the response to other forcing in the 20th century and with internal climate variability, despite attempts to minimize these effects—see discussion in North and Stevens (1998).

### Bars and Probability Density Functions

Otto et al. (2013) update the analysis of Gregory et al. (2002) and Gregory and Forster (2008) using forcing estimates from Forster et al. (2013) to obtain a 5 to 95% range for TCR of 0.9 to 2.0°C comparing the decade 2000–2009 with the period 1860–1879. They note, however, the danger of overinterpreting a single, possibly anomalous, decade, and report a larger TCR range of 0.7°C to 2.5°C replacing the 2000s with the 40 years 1970–2009. These PDFs are directly taken from Otto et al. (2013), renormalized to a (0.1 to 10) °C support.

Rogelj et al. (2012): This PDF is a TCR distribution implied by a 600-member parameter set ensemble drawn from an 82-dimensional parameter space in a way such that the posterior climate sensitivity distribution matches closely the distribution presented by Rogelj et al. (2012). The methodology for drawing the 600-member parameter sets is described in Meinshausen et al. (2009).

The PDF for the TCR predicted by the Bayesian methodology of Harris et al. (2013). The distribution is based upon a large sample of emulated General Circulation Model (GCM) equilibrium responses, constrained by multiannual mean observations of recent climate and adjusted to account for additional uncertainty associated with model structural deficiencies Sexton et al. (2012). The equilibrium responses are scaled by global temperature changes associated with the sampled model variants, reweighting the projections based on the likelihood that they correctly replicate observed historical changes in surface temperature, to predict the TCR distribution.

Meinshausen et al. (2009) compiled a large set of published marginal PDFs for equilibrium climate sensitivity (ECS) and TCR. In the absence of a formal method for combining all of them they chose an illustrative default, choosing a uniform TCR prior PDF from Frame et al. (2006) and constrained the their model parameter with observations. The TCR PDF is reproduced as shown in Figure 1b of the cited paper from supplementary data.

Knutti and Tomassini (2008) compare Earth System Model of Intermediate Complexity (EMIC) simulations with 20th century surface and ocean temperatures to derive a probability density function for TCR skewed slightly towards lower values with a 5 to 95% percent range of 1.1°C to 2.3°C. The PDFs for the expert ECS prior and the uniform ECS prior are reproduced as shown in Figure 1b of Meinshausen et al. (2009) from its supplementary data. The 5 to 95% confidence intervals are calculated from these numeric PDFs.

### Dashed Probability Density Functions without Legend Entries (AR4 Studies)

The TCR PDFs for the GFDL, the HadCM3, and the PCM model as produced by Stott et al. (2006) and the TCR PDF from Frame et al. (2006) are reproduced in Figure 10.19 as shown in Figure 1b of Meinshausen et al. (2009) from its supplementary data.

## Figure 10.20b

References for labelled plots: **20th Century:** violet: Aldrin et al. (2012), solid: uniform prior in ECS, dashed: uniform prior in 1/ECS, and dash-dotted is an update using data to 2010 (see below); gold: Bender et al. (2010); light red: Lewis (2013), dashed: using Forest et al. diagnostic and an objective Bayesian prior, solid using revised diagnostic; cyan: Lin et al. (2010); brown: Lindzen and Choi (2011); olive: Murphy et al., (2009); dark red: Olson et al. (2012); indigo: Otto et al. (2013), solid is an estimate using change to 1979–2009, dashed on the change to 2000–2009; lime: Schwartz (2012); blue: Tomassini et al. (2007) using a prior uniform in ECS (solid) and a density ratio prior based on expert elicitations (dashed). Repeated from AR4: green: Frame et al. (2005); result using uniform prior in ECS); orange: Gregory et al. (2002); purple: Knutti et al. (2002); Fuchsia: Forster and Gregory (2006) (solid: uniform prior in feedbacks; dashed transformed to uniform prior in ECS as used in AR4). **Palaeoclimate:** brown: (Chylek and Lohmann, 2008); orange: Hargreaves et al. (2012), solid, dashed showing an update based on PMIP3 simulations; turquoise: Holden et al. (2010); light red: Koehler et al. (2010); green: Paleosens Members (2012); purple: Schmittner et al. (2011), solid is land-and-ocean, dashed land-only, and dash-dotted is ocean-only diagnostic. Repeated from AR4: blue: Schneider von Deimling et al. (2006). lime: Annan et al. (2005); **Combination of evidence:** violet: Aldrin et al. (2012); turquoise: Libardoni and Forest (2013) with dashed being the average value, and solid an update using data to 2004; dark red: Olson et al. (2012) and repeated from AR4: lime: Annan and Hargreaves (2006); blue: Hegerl et al. (2006).

Processing details: All PDFs were scaled to integrate to 1.0 between 0 and 10.0; information only where further processing is used.

### Instrumental

Aldrin et al. (2012) Solid: Main result from the paper, that is, with data up to 2007 and with radiative forcing (RF)-prior consistent with the IPCC AR4; result from their Figure 6a; dashed Figure 6f; and in bottom panel Figure 6k. The dash-dotted is as the first, but updated including 2010 and with updated RF prior based on Skeie et al. (2011).

Lewis (2013) – two sets of data are used, based on their Figure 3, a and b.

Murphy (2009) – the 5th, 50th and 95th percentile are shown, based on published range for feedbacks in paper.

Olson et al. (2012) use a uniform and an informed prior. Here we plot the result of using a uniform prior, the informed prior is shown in the 'combination' panel.

Otto et al. (2013) – Two sets of data are used: in solid is the 1979–2009 average, and in dashed is the 2000–2009 average. Distributions are shown with percentiles coinciding with corresponding confidence intervals from the likelihood profile reported in the paper.

Schwartz (2012) – sampling range from their paper.

Frame et al. (2005) as in AR4.

Forster and Gregory (2006) – two sets of data are shown: in solid is data produced using a prior that is uniform in feedback parameter space, whilst in dashed is a prior that is uniform in ECS space. Data for the dashed curve was based on AR4; for the solid curve based on the feedback range given in the paper.

Knutti et al. (2002) – data was provided as cumulative distribution frequency, so binned to get probability distribution, applied a two-stage boxcar average (three-box window followed by two-box window), and rescaled to ensure integral of PDF equaled 1.0

### Palaeoclimate

Chylek and Lohmann (2008) (note range given is a 95% range).

Hargreaves et al. (2012) (solid: published estimate, dashed: updated).

Holden et al. (2010) – sampling range from their paper.

Schneider von Deimling et al. (2006) – sampling range from their paper.

### Combination

Aldrin et al. (2012) – result from their panel Figure 6k.

Libardoni and Forest (2013) (solid: published; dashed update using data to 2004).

Olson et al. (2012) – this is the main result of their paper, using an informed prior in ECS.

The average distribution given for Libardoni and Forest (2013) are calculated from an average of the PDFs based on different observational data sets; namely HadCRUT3, NCDC and GISTEMP250. The average distributions were derived by drawing Latin Hypercube samples from the posteriors derived using the different data sets. Three 1000-member samples were drawn from each, merged together, and the resulting histogram used to obtain an estimate of the average posterior; which was then smoothed and plotted.

## Additional Information to Version of Figure in Chapter 12

### Climatological Constraints

Red: Sexton et al. (2012) – purple: Knutti et al. (2006) – no processing was required. Gold: Piani et al. (2005).

Raw Model Range: The bars show the results from five perturbed physics ensembles. Each ensemble provided its histogram, computed using 0.5° bins. For ease of viewing, the individual bar widths have been shrunk by 7 (i.e., each bar appears as 0.071° of ECS in width, with a 0.14° gap between bins). The bar height has not been rescaled. The individual dots below the curve represent data from models in the CMIP3 and CMIP5 database. Not all models had completed the necessary simulations, so this is a subset of the full models available based on Table 9.5.

The CMIP5 models shown are:
ACCESS1-0, BCC-CSM1-1, BCC-CSM1-1-M, BNU-ESM, CanESM2, CCSM4,CNRM-CM5, CSIRO-Mk3-6-0, GFDL-CM3, GFDL-ESM2G, GFDL-ESM2M,GISS-E2-H, GISS-E2-R, HadGEM2-ES, INM-CM4, IPSL-CM5A-LR, IPSL-CM5B-LR,MIROC5, MIROC-ESM, MPI-ESM-LR, MPI-ESM-P, MRI-CGCM3, NorESM1-M.

Data for the AR4 AOGCMs was provided by Chapter 9, Table 9.5.

## Figure 10.21

This material documents the provenance of the data and plotting procedures that were used to create Figure 10.21 in the IPCC WG1 Fifth Assessment Report.

### Continental Temperatures

Models and ensemble members used are listed in Table 10.SM.5.

### Data

All of the data used were provided as monthly Netcdf files, from the CMIP3 and CMIP5 archives, and Daithi Stone (providing data used in the AR4 figures that were not in the CMIP3 archive). CMIP3 20C3M experiments were extended to 2012 by using A1B scenario simulations. CMIP5 historical experiments were extended to 2012 by using historicalExt and rcp45 experiments.

### Observational Data

The observed surface temperature data is from HadCRUT4 (Morice et al., 2012).

### Regridding

All data are re-gridded onto the HadCRUT4 spatial grid (5° × 5°) since HadCRUT4 generally has the most restricted spatial coverage of the datasets considered here. There is no infilling into grid boxes with no observations. The re-gridding is done by area averaging any part of the old grid that lies within the new grid to produce a new gridpoint value.

**Table 10.SM.5 |** Models and ensemble members used for continental temperatures. '20C2M' and 'A1B' are the names from CMIP3 for the quasi-equivalent experiments 'historical' and 'rcp45' in CMIP5.

| | historical (20C3M) | historicalExt | rcp45 (A1B) | Overall period | | | historicalNat | Overall period | | |
|---|---|---|---|---|---|---|---|---|---|---|
| Model | Realisation | Realisation | Realisation | Start Year | End Year | CMIP3/5 | Realisation | Start Year | End Year | CMIP3/5 |
| GFDL-CM2.0 | r1 | | r1 | 1861 | 2012 | 3 | | | | |
| GFDL-CM2.0 | r2 | | | 1861 | 2000 | 3 | | | | |
| GFDL-CM2.0 | r3 | | | 1861 | 2000 | 3 | | | | |
| GFDL-CM2.1 | r1 | | r3[a] | 1861 | 2012 | 3 | | | | |
| GFDL-CM2.1 | r2 | | r1 | 1861 | 2012 | 3 | | | | |
| GFDL-CM2.1 | r3 | | r2[a] | 1861 | 2012 | 3 | | | | |
| GFDL-CM2.1 | r4 | | | 1861 | 2000 | 3 | | | | |
| GFDL-CM2.1 | r5 | | | 1861 | 2000 | 3 | | | | |
| GISS-E-H | r1 | | r1 | 1880 | 2012 | 3 | | | | |
| GISS-E-H | r2 | | r2 | 1880 | 2012 | 3 | | | | |
| GISS-E-H | r3 | | r3 | 1880 | 2012 | 3 | | | | |
| GISS-E-H | r4 | | | 1880 | 1999 | 3 | | | | |
| GISS-E-H | r5 | | | 1880 | 1999 | 3 | | | | |
| GISS-E-R | r1 | | | 1880 | 2003 | 3 | | | | |
| GISS-E-R | r2 | | | 1880 | 2003 | 3 | | | | |
| GISS-E-R | r3 | | r1 | 1880 | 2012 | 3 | | | | |
| GISS-E-R | r4 | | | 1880 | 2003 | 3 | | | | |
| GISS-E-R | r5 | | | 1880 | 2003 | 3 | | | | |
| GISS-E-R | r6 | | r2 | 1880 | 2012 | 3 | | | | |
| GISS-E-R | r7 | | r3 | 1880 | 2012 | 3 | | | | |
| GISS-E-R | r8 | | r4 | 1880 | 2012 | 3 | | | | |
| GISS-E-R | r9 | | r5 | 1880 | 2012 | 3 | | | | |
| INM-CM3.0 | r1 | | r1 | 1871 | 2012 | 3 | | | | |
| MIROC3.2(hires) | r1 | | r1 | 1900 | 2012 | 3 | | | | |
| MIROC3.2(medres) | r1 | | r1 | 1850 | 2012 | 3 | r1 | 1850 | 2000 | 3 |
| MIROC3.2(medres) | r2 | | r2 | 1850 | 2012 | 3 | r2 | 1850 | 2000 | 3 |
| MIROC3.2(medres) | r3 | | r3 | 1850 | 2012 | 3 | r3 | 1850 | 2000 | 3 |
| MIROC3.2(medres) | r4[a] | | | 1850 | 2010 | 3 | r4 | 1850 | 2000 | 3 |
| MIROC3.2(medres) | r5[a] | | | 1850 | 2010 | 3 | r5 | 1850 | 2000 | 3 |
| MIROC3.2(medres) | r6[a] | | | 1850 | 2010 | 3 | r6 | 1850 | 2000 | 3 |
| MIROC3.2(medres) | r7 [a] | | | 1850 | 2010 | 3 | r7 | 1850 | 2000 | 3 |
| MIROC3.2(medres) | r8[a] | | | 1850 | 2010 | 3 | r8 | 1850 | 2000 | 3 |
| MIROC3.2(medres) | r9[a] | | | 1850 | 2010 | 3 | r9 | 1850 | 2000 | 3 |
| MIROC3.2(medres) | r10[a] | | | 1850 | 2010 | 3 | r10 | 1850 | 2000 | 3 |
| MIUB-ECHO-G | r1 | | r1 | 1860 | 2012 | 3 | r1 | 1860 | 2000 | 3 |
| MIUB-ECHO-G | r2 | | r2 | 1860 | 2012 | 3 | r2 | 1860 | 2000 | 3 |
| MIUB-ECHO-G | r3 | | r3 | 1860 | 2012 | 3 | r3 | 1860 | 2000 | 3 |
| MIUB-ECHO-G | r4 | | | 1860 | 2000 | 3 | | | | |
| MRI-CGCM2.3.2 | r1 | | | 1851 | 2000 | 3 | r1 | 1850 | 1999 | 3 |
| MRI-CGCM2.3.2 | r2 | | | 1851 | 2000 | 3 | r2 | 1850 | 1999 | 3 |
| MRI-CGCM2.3.2 | r3 | | | 1851 | 2000 | 3 | r3 | 1850 | 1999 | 3 |
| MRI-CGCM2.3.2 | r4 | | | 1851 | 2000 | 3 | r4 | 1850 | 2000 | 3 |
| MRI-CGCM2.3.2 | r5 | | | 1851 | 2000 | 3 | | | | |
| CCSM3 | r1 | | r1 | 1870 | 2012 | 3 | r1 | 1870 | 1999 | 3 |
| CCSM3 | r2 | | r2 | 1870 | 2012 | 3 | r2 | 1870 | 1999 | 3 |

*(continued on next page)*

*Table 10.SM.5 (continued)*

| | historical (20C3M) | historicalExt | rcp45 (A1B) | Overall period | | | historicalNat | Overall period | | |
|---|---|---|---|---|---|---|---|---|---|---|
| Model | Realisation | Realisation | Realisation | Start Year | End Year | CMIP3/5 | Realisation | Start Year | End Year | CMIP3/5 |
| CCSM3 | r3 | | r3 | 1870 | 2012 | 3 | r3 | 1870 | 1999 | 3 |
| CCSM3 | r4 | | | 1870 | 1999 | 3 | r4 | 1870 | 1999 | 3 |
| CCSM3 | r5 | | r5 | 1870 | 2012 | 3 | r5 | 1870 | 1999 | 3 |
| CCSM3 | r6 | | r6 | 1870 | 2012 | 3 | | | | |
| CCSM3 | r7 | | r7 | 1870 | 2012 | 3 | | | | |
| CCSM3 | r8 | | r8 | 1870 | 2011 | 3 | | | | |
| CCSM3 | r9 | | r9 | 1870 | 2012 | 3 | | | | |
| PCM | r1 | | | 1890 | 1999 | 3 | r1 | 1890 | 1999 | 3 |
| PCM | r2 | | | 1890 | 1999 | 3 | r2 | 1890 | 1999 | 3 |
| PCM | r3 | | | 1890 | 1999 | 3 | r3 | 1890 | 1999 | 3 |
| PCM | r4 | | | 1890 | 1999 | 3 | r4 | 1890 | 1999 | 3 |
| UKMO_HadCM3 | r1[a] | | | 1860 | 2006 | 3 | r1 | 1860 | 1998 | 3 |
| UKMO_HadCM3 | | | | | | | r2 | 1860 | 1998 | 3 |
| UKMO_HadCM3 | r3[a] | | | 1860 | 2002 | 3 | r3 | 1860 | 1998 | 3 |
| UKMO_HadCM3 | r4[a] | | | 1860 | 2002 | 3 | r4 | 1860 | 1998 | 3 |
| UKMO_HadGEM1 | r1[a] | | | 1860 | 2009 | 3 | | | | |
| UKMO_HadGEM1 | r2[a] | | | 1860 | 2009 | 3 | | | | |
| UKMO_HadGEM1 | r3[a] | | | 1860 | 2009 | 3 | | | | |
| UKMO_HadGEM1 | r4[a] | | | 1860 | 2009 | 3 | | | | |
| ACCESS1.0 | r1i1p1 | | r1i1p1 | 1850 | 2012 | 5 | | | | |
| ACCESS1.3 | r1i1p1 | | r1i1p1 | 1850 | 2012 | 5 | | | | |
| ACCESS1.3 | r2i1p1 | | | 1850 | 2005 | 5 | | | | |
| ACCESS1.3 | r3i1p1 | | | 1850 | 2005 | 5 | | | | |
| BNU-ESM | r1i1p1 | | r1i1p1 | 1850 | 2012 | 5 | r1i1p1 | 1850 | 2005 | 5 |
| CCSM4 | r1i1p1 | | r1i1p1 | 1850 | 2012 | 5 | r1i1p1 | 1850 | 2005 | 5 |
| CCSM4 | r2i1p1 | | r2i1p1 | 1850 | 2012 | 5 | r2i1p1 | 1850 | 2005 | 5 |
| CCSM4 | r3i1p1 | | r3i1p1 | 1850 | 2012 | 5 | | | | |
| CCSM4 | r4i1p1 | | r4i1p1 | 1850 | 2012 | 5 | r4i1p1 | 1850 | 2005 | 5 |
| CCSM4 | r5i1p1 | | r5i1p1 | 1850 | 2012 | 5 | | | | |
| CCSM4 | r6i1p1 | | r6i1p1 | 1850 | 2012 | 5 | r6i1p1 | 1850 | 2005 | 5 |
| CESM1(BGC) | r1i1p1 | | r1i1p1 | 1850 | 2012 | 5 | | | | |
| CESM1(CAM5) | r1i1p1 | | r1i1p1 | 1850 | 2012 | 5 | | | | |
| CESM1(CAM5) | r2i1p1 | | r2i1p1 | 1850 | 2012 | 5 | | | | |
| CESM1(CAM5) | r3i1p1 | | r3i1p1 | 1850 | 2012 | 5 | | | | |
| CESM1(FASTCHEM) | r1i1p1 | | | 1850 | 2005 | 5 | | | | |
| CESM1(FASTCHEM) | r2i1p1 | | | 1850 | 2005 | 5 | | | | |
| CESM1(FASTCHEM) | r3i1p1 | | | 1850 | 2005 | 5 | | | | |
| CESM1(WACCM) | r1i1p1 | | | 1850 | 2005 | 5 | | | | |
| CMCC-CESM | r1i1p1 | | | 1850 | 2005 | 5 | | | | |
| CMCC-CMS | r1i1p1 | | r1i1p1 | 1850 | 2012 | 5 | | | | |
| CMCC-CM | r1i1p1 | | r1i1p1 | 1850 | 2012 | 5 | | | | |
| CNRM-CM5 | r1i1p1 | r1i1p1 | | 1850 | 2012 | 5 | r1i1p1 | 1850 | 2012 | 5 |
| CNRM-CM5 | r2i1p1 | r2i1p1 | | 1850 | 2012 | 5 | r2i1p1 | 1850 | 2012 | 5 |
| CNRM-CM5 | r3i1p1 | r3i1p1 | | 1850 | 2012 | 5 | r3i1p1 | 1850 | 2012 | 5 |
| CNRM-CM5 | r4i1p1 | r4i1p1 | | 1850 | 2012 | 5 | r4i1p1 | 1850 | 2012 | 5 |
| CNRM-CM5 | r5i1p1 | r5i1p1 | | 1850 | 2012 | 5 | r5i1p1 | 1850 | 2012 | 5 |

*(continued on next page)*

*Table 10.SM.5 (continued)*

| | historical (20C3M) | historicalExt | rcp45 (A1B) | Overall period | | | historicalNat | Overall period | | |
|---|---|---|---|---|---|---|---|---|---|---|
| **Model** | **Realisation** | **Realisation** | **Realisation** | **Start Year** | **End Year** | **CMIP3/5** | **Realisation** | **Start Year** | **End Year** | **CMIP3/5** |
| CNRM-CM5 | r6i1p1 | r6i1p1 | | 1850 | 2012 | 5 | | | | |
| CNRM-CM5 | r7i1p1 | r7i1p1 | | 1850 | 2012 | 5 | | | | |
| CNRM-CM5 | r8i1p1 | r8i1p1 | | 1850 | 2012 | 5 | r8i1p1 | 1850 | 2012 | 5 |
| CNRM-CM5 | r9i1p1 | r9i1p1 | | 1850 | 2012 | 5 | | | | |
| CNRM-CM5 | r10i1p1 | r10i1p1 | | 1850 | 2012 | 5 | | | | |
| CSIRO-Mk3.6.0 | r1i1p1 | | r1i1p1 | 1850 | 2012 | 2012 | r1i1p1 | 1850 | 2012 | **5** |
| CSIRO-Mk3.6.0 | r2i1p1 | | r2i1p1 | 1850 | 2012 | 5 | r2i1p1 | 1850 | 2012 | 5 |
| CSIRO-Mk3.6.0 | r3i1p1 | | r3i1p1 | 1850 | 2012 | 5 | r3i1p1 | 1850 | 2012 | 5 |
| CSIRO-Mk3.6.0 | r4i1p1 | | r4i1p1 | 1850 | 2012 | 5 | r4i1p1 | 1850 | 2012 | 5 |
| CSIRO-Mk3.6.0 | r5i1p1 | | r5i1p1 | 1850 | 2012 | 5 | r5i1p1 | 1850 | 2012 | 5 |
| CSIRO-Mk3.6.0 | r6i1p1 | | r6i1p1 | 1850 | 2012 | 5 | | | | |
| CSIRO-Mk3.6.0 | r7i1p1 | | r7i1p1 | 1850 | 2012 | 5 | | | | |
| CSIRO-Mk3.6.0 | r8i1p1 | | r8i1p1 | 1850 | 2012 | 5 | | | | |
| CSIRO-Mk3.6.0 | r9i1p1 | | r9i1p1 | 1850 | 2012 | 5 | | | | |
| CSIRO-Mk3.6.0 | r10i1p1 | | r10i1p1 | 1850 | 2012 | 5 | | | | |
| CanESM2 | r1i1p1 | r1i1p1 | | 1850 | 2012 | 5 | r1i1p1 | 1850 | 2012 | 5 |
| CanESM2 | r2i1p1 | r2i1p1 | | 1850 | 2012 | 5 | r2i1p1 | 1850 | 2012 | 5 |
| CanESM2 | r3i1p1 | r3i1p1 | | 1850 | 2012 | 5 | r3i1p1 | 1850 | 2012 | 5 |
| CanESM2 | r4i1p1 | r4i1p1 | | 1850 | 2012 | 5 | r4i1p1 | 1850 | 2012 | 5 |
| CanESM2 | r5i1p1 | r5i1p1 | | 1850 | 2012 | 5 | r5i1p1 | 1850 | 2012 | 5 |
| EC-EARTH | r1i1p1 | | r1i1p1 | 1850 | 2012 | 5 | | | | |
| EC-EARTH | r2i1p1 | | r2i1p1 | 1850 | 2012 | 5 | | | | |
| EC-EARTH | r6i1p1 | | r6i1p1 | 1850 | 2012 | 5 | | | | |
| EC-EARTH | r8i1p1 | | r8i1p1 | 1850 | 2012 | 5 | | | | |
| EC-EARTH | r9i1p1 | | r9i1p1 | 1850 | 2012 | 5 | | | | |
| EC-EARTH | r11i1p1 | | | 1850 | 2012 | 5 | | | | |
| EC-EARTH | r12i1p1 | | r12i1p1 | 1850 | 2012 | 5 | | | | |
| FIO-ESM | r1i1p1 | | r1i1p1 | 1850 | 2012 | 5 | | | | |
| FIO-ESM | r2i1p1 | | r2i1p1 | 1850 | 2012 | 5 | | | | |
| FIO-ESM | r3i1p1 | | r3i1p1 | 1850 | 2012 | 5 | | | | |
| GFDL-CM2p1 | r1i1p1 | | | 1861 | 2012 | 5 | | | | |
| GFDL-CM2p1 | r2i1p1 | | | 1861 | 2012 | 5 | | | | |
| GFDL-CM2p1 | r3i1p1 | | | 1861 | 2012 | 5 | | | | |
| GFDL-CM2p1 | r4i1p1 | | | 1861 | 2012 | 5 | | | | |
| GFDL-CM2p1 | r5i1p1 | | | 1861 | 2012 | 5 | | | | |
| GFDL-CM2p1 | r6i1p1 | | | 1861 | 2012 | 5 | | | | |
| GFDL-CM2p1 | r7i1p1 | | | 1861 | 2012 | 5 | | | | |
| GFDL-CM2p1 | r8i1p1 | | | 1861 | 2012 | 5 | | | | |
| GFDL-CM2p1 | r9i1p1 | | | 1861 | 2012 | 5 | | | | |
| GFDL-CM2p1 | r10i1p1 | | | 1861 | 2012 | 5 | | | | |
| GFDL-CM3 | r1i1p1 | | r1i1p1 | 1860 | 2012 | 5 | r1i1p1 | 1860 | 2005 | 5 |
| GFDL-CM3 | r2i1p1 | | | 1860 | 2005 | 5 | | | | |
| GFDL-CM3 | r3i1p1 | | | 1860 | 2005 | 5 | r3i1p1 | 1860 | 2005 | 5 |
| GFDL-CM3 | r4i1p1 | | | 1860 | 2005 | 5 | | | | |
| GFDL-CM3 | r5i1p1 | | | 1860 | 2005 | 5 | r5i1p1 | 1860 | 2005 | 5 |
| GFDL-ESM2G | r1i1p1 | | r1i1p1 | 1861 | 2012 | 5 | | | | |
| GFDL-ESM2M | r1i1p1 | | r1i1p1 | 1861 | 2012 | 5 | r1i1p1 | 1861 | 2005 | 5 |

*(continued on next page)*

*Table 10.SM.5 (continued)*

| | historical (20C3M) | historicalExt | rcp45 (A1B) | Overall period | | | historicalNat | Overall period | | |
|---|---|---|---|---|---|---|---|---|---|---|
| **Model** | **Realisation** | **Realisation** | **Realisation** | **Start Year** | **End Year** | **CMIP3/5** | **Realisation** | **Start Year** | **End Year** | **CMIP3/5** |
| GISS-E2-H-CC | r1i1p1 | | r1i1p1 | 1850 | 2012 | 5 | | | | |
| GISS-E2-H | r1i1p1 | r1i1p1 | | 1850 | 2012 | 5 | r1i1p1 | 1850 | 2012 | 5 |
| GISS-E2-H | r2i1p1 | r2i1p1 | | 1850 | 2012 | 5 | r2i1p1 | 1850 | 2012 | 5 |
| GISS-E2-H | r3i1p1 | r3i1p1 | | 1850 | 2012 | 5 | r3i1p1 | 1850 | 2012 | 5 |
| GISS-E2-H | r4i1p1 | r4i1p1 | | 1850 | 2012 | 5 | r4i1p1 | 1850 | 2012 | 5 |
| GISS-E2-H | r5i1p1 | r5i1p1 | | 1850 | 2012 | 5 | r5i1p1 | 1850 | 2012 | 5 |
| GISS-E2-H | r6i1p1 | | | 1850 | 2012 | 5 | | | | |
| GISS-E2-R-CC | r1i1p1 | | r1i1p1 | 1850 | 2012 | 5 | | | | |
| GISS-E2-R | r1i1p1 | r1i1p1 | | 1850 | 2012 | 5 | r1i1p1 | 1850 | 2012 | 5 |
| GISS-E2-R | r2i1p1 | r2i1p1 | | 1850 | 2012 | 5 | r2i1p1 | 1850 | 2012 | 5 |
| GISS-E2-R | r3i1p1 | r3i1p1 | | 1850 | 2012 | 5 | r3i1p1 | 1850 | 2012 | 5 |
| GISS-E2-R | r4i1p1 | r4i1p1 | | 1850 | 2012 | 5 | r4i1p1 | 1850 | 2012 | 5 |
| GISS-E2-R | r5i1p1 | r5i1p1 | | 1850 | 2012 | 5 | r5i1p1 | 1850 | 2012 | 5 |
| GISS-E2-R | r6i1p1 | | r6i1p1 | 1850 | 2012 | 5 | | | | |
| HadCM3 | r1i1p1 | | r1i1p1 | 1860 | 2012 | 5 | | | | |
| HadCM3 | r2i1p1 | | r2i1p1 | 1860 | 2012 | 5 | | | | |
| HadCM3 | r3i1p1 | | r3i1p1 | 1860 | 2012 | 5 | | | | |
| HadCM3 | r4i1p1 | | r4i1p1 | 1860 | 2012 | 5 | | | | |
| HadCM3 | r5i1p1 | | r5i1p1 | 1860 | 2012 | 5 | | | | |
| HadCM3 | r6i1p1 | | r6i1p1 | 1860 | 2012 | 5 | | | | |
| HadCM3 | r7i1p1 | | r7i1p1 | 1860 | 2012 | 5 | | | | |
| HadCM3 | r8i1p1 | | r8i1p1 | 1860 | 2012 | 5 | | | | |
| HadCM3 | r9i1p1 | | r9i1p1 | 1860 | 2012 | 5 | | | | |
| HadCM3 | r10i1p1 | | r10i1p1 | 1860 | 2012 | 5 | | | | |
| HadGEM2-AO | r1i1p1 | | r1i1p1 | 1860 | 2012 | 5 | | | | |
| HadGEM2-CC | r1i1p1 | | r1i1p1 | 1860 | 2012 | 5 | | | | |
| HadGEM2-ES | r1i1p1 | | r1i1p1 | 1860 | 2012 | 5 | r1i1p1 | 1860 | 2012 | 5 |
| HadGEM2-ES | r2i1p1 | r2i1p1 | | 1860 | 2012 | 5 | r2i1p1 | 1860 | 2012 | 5 |
| HadGEM2-ES | r3i1p1 | r3i1p1 | | 1860 | 2012 | 5 | r3i1p1 | 1860 | 2012 | 5 |
| HadGEM2-ES | r4i1p1 | r4i1p1 | | 1860 | 2012 | 5 | r4i1p1 | 1860 | 2012 | 5 |
| HadGEM2-ES | r5i1p1 | | | 1860 | 2005 | 5 | | | | |
| IPSL-CM5A-LR | r1i1p1 | | r1i1p1 | 1850 | 2012 | 5 | r1i1p1 | 1850 | 2012 | 5 |
| IPSL-CM5A-LR | r2i1p1 | | r2i1p1 | 1850 | 2012 | 5 | r2i1p1 | 1850 | 2012 | 5 |
| IPSL-CM5A-LR | r3i1p1 | | r3i1p1 | 1850 | 2012 | 5 | r3i1p1 | 1850 | 2012 | 5 |
| IPSL-CM5A-LR | r4i1p1 | | r4i1p1 | 1850 | 2012 | 5 | | | | |
| IPSL-CM5A-LR | r5i1p1 | | | 1850 | 2005 | 5 | | | | |
| IPSL-CM5A-LR | r6i1p1 | | | 1850 | 2005 | 5 | | | | |
| IPSL-CM5A-MR | r1i1p1 | | r1i1p1 | 1850 | 2012 | 5 | r1i1p1 | 1850 | 2012 | 5 |
| IPSL-CM5A-MR | r2i1p1 | | | 1850 | 2005 | 5 | r2i1p1 | 1850 | 2012 | 5 |
| IPSL-CM5A-MR | r3i1p1 | | | 1850 | 2005 | 5 | r3i1p1 | 1850 | 2012 | 5 |
| IPSL-CM5B-LR | r1i1p1 | | r1i1p1 | 1850 | 2012 | 5 | | | | |
| MIROC-ESM-CHEM | r1i1p1 | | r1i1p1 | 1850 | 2012 | 5 | r1i1p1 | 1850 | 2005 | 5 |
| MIROC-ESM | r1i1p1 | | r1i1p1 | 1850 | 2012 | 5 | r1i1p1 | 1850 | 2005 | 5 |
| MIROC-ESM | r2i1p1 | | | 1850 | 2005 | 5 | r2i1p1 | 1850 | 2005 | 5 |
| MIROC-ESM | r3i1p1 | | | 1850 | 2005 | 5 | r3i1p1 | 1850 | 2005 | 5 |
| MIROC5 | r1i1p1 | | r1i1p1 | 1850 | 2012 | 5 | | | | |
| MIROC5 | r2i1p1 | | r2i1p1 | 1850 | 2012 | 5 | | | | |

*(continued on next page)*

*Table 10.SM.5 (continued)*

| | historical (20C3M) | historicalExt | rcp45 (A1B) | Overall period | | | historicalNat | Overall period | | |
|---|---|---|---|---|---|---|---|---|---|---|
| **Model** | **Realisation** | **Realisation** | **Realisation** | **Start Year** | **End Year** | **CMIP3/5** | **Realisation** | **Start Year** | **End Year** | **CMIP3/5** |
| MIROC5 | r3i1p1 | | r3i1p1 | 1850 | 2012 | 5 | | | | |
| MIROC5 | r4i1p1 | | | 1850 | 2012 | 5 | | | | |
| MIROC5 | r5i1p1 | | | 1850 | 2012 | 5 | | | | |
| MPI-ESM-LR | r1i1p1 | | r1i1p1 | 1850 | 2012 | 5 | | | | |
| MPI-ESM-LR | r2i1p1 | | r2i1p1 | 1850 | 2012 | 5 | | | | |
| MPI-ESM-LR | r3i1p1 | | r3i1p1 | 1850 | 2012 | 5 | | | | |
| MPI-ESM-MR | r1i1p1 | | r1i1p1 | 1850 | 2012 | 5 | | | | |
| MPI-ESM-MR | r2i1p1 | | r2i1p1 | 1850 | 2012 | 5 | | | | |
| MPI-ESM-MR | r3i1p1 | | r3i1p1 | 1850 | 2012 | 5 | | | | |
| MPI-ESM-P | r1i1p1 | | | 1850 | 2005 | 5 | | | | |
| MPI-ESM-P | r2i1p1 | | | 1850 | 2005 | 5 | | | | |
| MRI-CGCM3 | r1i1p1 | r1i1p1 | | 1850 | 2012 | 5 | r1i1p1 | 1850 | 2005 | 5 |
| MRI-CGCM3 | r2i1p1 | r2i1p1 | | 1850 | 2012 | 5 | | | | |
| MRI-CGCM3 | r3i1p1 | r3i1p1 | | 1850 | 2012 | 5 | | | | |
| MRI-ESM1 | r1i1p1 | | | 1851 | 2005 | 5 | | | | |
| NorESM1-ME | r1i1p1 | | r1i1p1 | 1850 | 2012 | 5 | r1i1p1 | 1850 | 2012 | 5 |
| NorESM1-M | r1i1p1 | r1i1p1 | | 1850 | 2012 | 5 | | | | |
| NorESM1-M | r2i1p1 | r2i1p1 | | 1850 | 2012 | 5 | | | | |
| NorESM1-M | r3i1p1 | r3i1p1 | | 1850 | 2012 | 5 | | | | |
| BCC-CSM1.1(m) | r1i1p1 | | r1i1p1 | 1850 | 2012 | 5 | | | | |
| BCC-CSM1.1(m) | r2i1p1 | | | 1850 | 2012 | 5 | | | | |
| BCC-CSM1.1(m) | r3i1p1 | | | 1850 | 2012 | 5 | | | | |
| BCC-CSM1.1 | r1i1p1 | | r1i1p1 | 1850 | 2012 | 5 | r1i1p1 | 1850 | 2012 | 5 |
| BCC-CSM1.1 | r2i1p1 | | | 1850 | 2012 | 5 | | | | |
| BCC-CSM1.1 | r3i1p1 | | | 1850 | 2012 | 5 | | | | |
| INM-CM4 | r1i1p1 | | r1i1p1 | 1850 | 2012 | 5 | | | | |

Notes:

[a] Simulation not in CMIP3 archive. Obtained from model institution or Daithi Stone (as used in figures in IPCC WG1 2007)

### Masking

The data coverage is limited to where data exists in the equivalent month/gridpoint of HadCRUT4. Note that this shortens some model time series (e.g., Antarctica).

### Multi-Model Mean

All ensemble members of a specific simulation of a specific model are averaged into an ensemble mean for a specific simulation and model before the models are averaged into a multi-model mean (details in supplementary material to Jones et al., 2013). Therewith, models with more ensemble members are not weighted disproportional to models with less ensemble members.

### Creation of Annual Means

Anomalies are calculated for each month/gridpoint relative to the 1880–1919 average (except Antarctica where anomalies are relative to 1950–2010), where at least 50% of the data in the reference period are needed to calculate the average. Annual means are calculated from monthly data for each calendar year, where at least 2 months are non-missing. Shadings are the 5 and 95 percentile among the models.

### Global Means

Global and regional mean anomalies are calculated by area averaging all available gridpoint data for each year.

### Regions

Continental land areas are based on the SREX defined regions (IPCC, 2012) shown pictorially in the bottom right most panel of Figure 10.7.

## Precipitation

Models and ensemble members used are listed in Table 10.SM.6.

### Data and Region

50°N–90°N average changes in annual mean precipitation (in mm day$^{-1}$) for the period 1951–2005, with regard to the baseline period of 1961–1990, are plotted based on Balan Sarojini et al. (2012).

### Observational Data

The first observational dataset used (black solid line) is a gridded observational dataset based on station data extracted from the Global

**Table 10.SM.6 |** Models and ensemble members used for precipitation.

| | historicalNat | Overall period | | historical | Overall period | | |
|---|---|---|---|---|---|---|---|
| **Model** | **Realisation** | **Start Year** | **End Year** | **Realisation** | **Start Year** | **End Year** | **CMIP3/5** |
| ACCESS1.0 | | | | r1i1p1 | 1951 | 2005 | 5 |
| BCC-CSM1.1 | r1i1p1 | 1951 | 2005 | r1i1p1 | 1951 | 2005 | 5 |
| CanESM2 | r1i1p1 | 1951 | 2005 | r1i1p1 | 1951 | 2005 | 5 |
| CCSM4 | | | | r1i1p1 | 1951 | 2005 | 5 |
| CESM1(BGC) | | | | r1i1p1 | 1951 | 2005 | 5 |
| CESM1(CAM5) | | | | r1i1p1 | 1951 | 2005 | 5 |
| CESM1 (FASTCHEM) | | | | r1i1p1 | 1951 | 2005 | 5 |
| CESM1(WACCM) | | | | r1i1p1 | 1951 | 2005 | 5 |
| CMCC-CESM | | | | r1i1p1 | 1951 | 2005 | 5 |
| CMCC-CMS | | | | r1i1p1 | 1951 | 2005 | 5 |
| CNRM-CM5 | r1i1p1 | 1951 | 2005 | r1i1p1 | 1951 | 2005 | 5 |
| CSIRO-Mk3.6.0 | r1i1p1 | 1951 | 2005 | r1i1p1 | 1951 | 2005 | 5 |
| GFDL-CM3 | r1i1p1 | 1951 | 2005 | r1i1p1 | 1951 | 2005 | 5 |
| GFDL-ESM2G | | | | r1i1p1 | 1951 | 2005 | 5 |
| GFDL-ESM2M | | | | r1i1p1 | 1951 | 2005 | 5 |
| GISS-E2-H | | | | r1i1p1 | 1951 | 2005 | 5 |
| GISS-E2-R | | | | r1i1p1 | 1951 | 2005 | 5 |
| HadGEM2-CC | | | | r1i1p1 | 1951 | 2005 | 5 |
| HadGEM2-ES | r1i1p1 | 1850 | 2005 | r1i1p1 | 1850 | 2005 | 5 |
| INMCM4_ESM | | | | r1i1p1 | 1850 | 2005 | 5 |
| IPSL-CM5A-LR | | | | r1i1p1 | 1850 | 2005 | 5 |
| IPSL-CM5A-MR | | | | r1i1p1 | 1951 | 2005 | 5 |
| MIROC5 | | | | r1i1p1 | 1951 | 2005 | 5 |
| MIROC-ESM | r1i1p1 | 1951 | 2005 | r1i1p1 | 1951 | 2005 | 5 |
| MIROC-ESM-CHEM | r1i1p1 | 1951 | 2005 | r1i1p1 | 1951 | 2005 | 5 |
| MPI-ESM-LR | | | | r1i1p1 | 1951 | 2005 | 5 |
| MPI-ESM-MR | | | | r1i1p1 | 1951 | 2005 | 5 |
| MRI-CGCM3 | r1i1p1 | 1951 | 2005 | r1i1p1 | 1951 | 2005 | 5 |
| NorESM1-M | r1i1p1 | 1951 | 2005 | r1i1p1 | 1951 | 2005 | 5 |
| NorESM1-ME | | | | r1i1p1 | 1951 | 2005 | 5 |

Historical Climatology Network (updated from Zhang et al., 2007). Monthly data for the period 1951–2005, quality controlled and gridded at 5° × 5°, for all land grid squares on the globe for which station data are available, are used. In order to avoid artefacts arising from changes in data coverage, a sampling criterion of choosing data available for >90% of the analysis period is applied (i.e., each spatial grid point is chosen when data over 90% of the years (only those years which have data for all months) are present).

The second observational dataset (grey solid line) used is a gridded observational dataset based on station data extracted from the Climatic Research Unit, (updated from CRU TS3.1 of Harris et al., 2013) and sampled as in Polson et al. (2013). Monthly data for the period 1951–2005, quality controlled and gridded at 0.5° × 0.5°, are used. This data is first interpolated to the common spatial resolution of 5° × 5°. In order to avoid artefacts arising from changes in data coverage, two sampling criteria are applied: 1) station sampling criterion (Polson et al., 2013) of choosing only those 5° × 5° grid boxes that have at least 1 station (in any 0.5° × 0.5° grid box) for the coastal grid boxes and with at least 2 stations for the inland grid boxes. A 5° × 5° grid box is coastal when over half of number of the 0.5° × 0.5° boxes is ocean points. 2) a criterion of choosing data available for >95% of the analysis period is applied. i.e., each spatial grid point is chosen when data over 95% of the years (years which have data available for any no of months) are present.

### Masking of Simulated Data onto the Observational Grid

First, the land area of the simulated data available in different spatial resolutions is obtained by choosing a grid point as land when its land-area fraction is greater than or equal to 70%. Second, the simulated land data are interpolated to the 5° × 5° observational grid using bi-linear interpolation. Third, the 90% sampling criterion derived from the observations is applied to each regridded model data to obtain the consistent temporal and spatial data coverage for the simulated and observed data.

### Calculation of Spatial and Annual Averages and Anomalies with regard to the Baseline Climatology

For each (regridded and sampled) monthly model data, spatial averages are first calculated for the zonal band of 50°N–90°N. Annual averages, baseline climatology (for 1961–1990) and anomalies from the baseline period are then calculated.

### Plotting

The yearly anomalies are plotted with a y-axis range of 1950–2010. Multi-model means are in thick solid lines (historical in red and historicalNat in blue).

The 5-95% confidence interval of the models is in pink shading for historical runs and in blue shading for historicalNat runs.

## Ocean Heat Content

Models and ensemble members used are listed in Table 10.SM.7.

### Observational Data

Three observational data sets are updated from Domingues et al. (2008), Levitus et al. (2012) and sourced from http://www.nodc.noaa.gov/OC5/3M_HEAT_CONTENT/index.html and Ishii and Kimoto (2009) and sourced from http://www.data.kishou.go.jp/kaiyou/english/ohc/ohc_data_en.html (version August 2012).

### Data Treatment

Before computing the ocean heat content the model output has been treated as in Pierce et al. (2012), i.e., horizontal regridding to a 10° x 10° latitude/longitude grid between 60°S and 60°N over the top 700 m; masking the grid boxes that lack observations; fields are de-drifted using second order polynomials fit to the pre-industrial control runs ('piControl').

Annual mean OHC values are calculated from models by vertically integrating the annual mean temperature anomalies (with respect to a 1960–1980 reference period). Global mean time series are calculated by integrating over space.

All OHC time series are relative to the reference period of 1960–1980. Only Domingues et al. (2008) OHC data are smoothed with a three-year running means.

### Regions

Ocean basin definition (Latitudes) are:

- Southern Ocean: south of 50°S
- South Pacific: 50°S to Equator
- South Atlantic : 50°S to Equator; up to 20°E;
- Indian Ocean: 50°S to 30°N; 20°E to Australia (Tasmania)
- North Pacific, North Atlantic: Equator to 70°N

## Sea Ice

September sea ice extent (concentration >15%) anomalies for the Northern Hemisphere (Arctic) and Southern Hemisphere (Antarctic), relative to 1979–1999. Models and ensemble members used for the final figure are listed in Table 10.SM.8. Observational data is from NSIDC bootstrap algorithm (SBA; Cavalieri and Parkinson, 2012; Parkinson and Cavalieri, 2012).

The historical simulations are extended with rcp85 to the year 2012. For both the historicalNat and historical extended with rcp85 the multi-model mean and 5–95% confidence interval for each year are calculated from all models available for that year.

**Table 10.SM.7 |** Models and ensemble members used for ocean heat content.

| | historicalNat | Overall period | | historical | Overall period | | |
|---|---|---|---|---|---|---|---|
| **Model** | **Realisation** | **Start Year** | **End Year** | **Realisation** | **Start Year** | **End Year** | **CMIP3/5** |
| CanESM2 | r1i1p1 | 1950 | 2012 | r1i1p1 | 1950 | 2005 | 5 |
| CCSM4 | r1i1p1 | 1950 | 2005 | r1i1p1 | 1950 | 2005 | 5 |
| CNRM-CM5 | r1i1p1 | 1950 | 2012 | r1i1p1 | 1950 | 2005 | 5 |
| CSIRO-MK3.6.0 | r1i1p1 | 1950 | 2012 | r1i1p1 | 1950 | 2005 | 5 |
| GISS-E2-H | r1i1p1 | 1950 | 2012 | r1i1p1 | 1950 | 2005 | 5 |
| GISS-E2-R | r1i1p1 | 1950 | 2012 | r1i1p1 | 1950 | 2005 | 5 |
| HADGEM2-ES | r1i1p1 | 1950 | 2012 | r1i1p1 | 1950 | 2003 | 5 |
| MIROC5 | | | | r1i1p1 | 1950 | 2005 | 5 |
| MIROC-ESM | r1i1p1 | 1950 | 2005 | r1i1p1 | 1950 | 2005 | 5 |
| MPI-ESM-LR | | | | r1i1p1 | 1950 | 2005 | 5 |
| MRI-CGCM3 | r1i1p1 | 1950 | 2005 | r1i1p1 | 1950 | 2005 | 5 |
| NorESM1-M | r1i1p1 | 1950 | 2005 | r1i1p1 | 1950 | 2005 | 5 |

The simulations have been plotted as anomalies from the mean for the reference period (1979–1999) with 5-95% confidence interval of the models as shading. The observations are the September sea ice extent anomalies relative to 1979–1999 period mean from the NSIDC sea-ice data set.

### Data Quality

For land and ocean surface temperatures and precipitation panels, solid green lines at bottom of panels indicate where data spatial coverage, of areas being examined, is above 50% coverage and dashed green lines where coverage is below 50%. For example, data coverage of Antarctica never goes above 50% of the land area of the continent. For ocean heat content and sea-ice panels the solid line is where the coverage of data is good and higher in quality, and the dashed line is where the data coverage is only adequate, based on a qualitative expert assessment. See the Table 10.SM.9 for the years of change from adequate to higher quality data.

**Table 10.SM.8 |** Models and ensemble members used for sea ice.

| | historicalNat | Overall period | | historical | rcp85 | Overall period | | |
|---|---|---|---|---|---|---|---|---|
| **Model** | **Realisation** | **Start Year** | **End Year** | **Realisation** | **Realisation** | **Start Year** | **End Year** | **CMIP3/5** |
| BCC-CSM1.1 | r1i1p1 | 1950 | 2012 | r1i1p1 | r1i1p1 | 1950 | 2012 | 5 |
| BNU-ESM | r1i1p1 | 1950 | 2005 | r1i1p1 | r1i1p1 | 1950 | 2012 | 5 |
| CanESM2 | r1i1p1 | 1950 | 2012 | r1i1p1 | r1i1p1 | 1950 | 2012 | 5 |
| CCSM4 | r1i1p1 | 1950 | 2005 | r1i1p1 | r1i1p1 | 1950 | 2012 | 5 |
| CNRM-CM5 | r1i1p1 | 1950 | 2012 | r1i1p1 | r1i1p1 | 1950 | 2012 | 5 |
| CSIRO-MK3.6.0 | r1i1p1 | 1950 | 2012 | r1i1p1 | r1i1p1 | 1950 | 2012 | 5 |
| FGOALS-g2 | r1i1p1 | 1950 | 2009 | r1i1p1 | r1i1p1 | 1950 | 2012 | 5 |
| GFDL-ESM2M | r1i1p1 | 1950 | 2005 | r1i1p1 | r1i1p1 | 1950 | 2012 | 5 |
| GISS-E2-H | r1i1p1 | 1950 | 2012 | r1i1p1 | r1i1p1 | 1950 | 2012 | 5 |
| GISS-E2-R | r1i1p1 | 1950 | 2012 | r1i1p1 | r1i1p1 | 1950 | 2012 | 5 |
| HADGEM2-ES | r1i1p1 | 1950 | 2012 | r1i1p1 | r1i1p1 | 1950 | 2012 | 5 |
| IPSL-CM5A-LR | r1i1p1 | 1950 | 2012 | r1i1p1 | r1i1p1 | 1950 | 2012 | 5 |
| IPSL-CM5A-MR | r1i1p1 | 1950 | 2012 | r1i1p1 | r1i1p1 | 1950 | 2012 | 5 |
| MIROC-ESM | r1i1p1 | 1950 | 2005 | r1i1p1 | r1i1p1 | 1950 | 2012 | 5 |
| MIROC-ESM-CHEM | r1i1p1 | 1950 | 2005 | r1i1p1 | r1i1p1 | 1950 | 2012 | 5 |
| MRI-CGCM3 | r1i1p1 | 1950 | 2005 | r1i1p1 | r1i1p1 | 1950 | 2012 | 5 |
| NorESM1-M | r1i1p1 | 1950 | 2012 | r1i1p1 | r1i1p1 | 1950 | 2012 | 5 |

**Table 10.SM.9 |** Years of change from adequate to higher quality data, i.e., when dashed lines change to solid lines.

| Element of climate system | Region | Year of change from dashed to solid line |
|---|---|---|
| Continental temperatures | Global Land+Ocean | 1880 |
| | Global Land | 1930 |
| | Global Ocean | 1880 |
| | North America | 1910 |
| | South America | 1930 |
| | Europe | 1860 |
| | Africa | 1950 |
| | Asia | 1925 |
| | Australia | 1910 |
| | Antarctica | 1944 |
| | | |
| Ocean Heat Content | All basins | 1970 |
| | | |
| Sea Ice | Arctic and Antarctica | 1979 |
| | | |
| Precipitation | Precipitation | 1985 |

## FAQ 10.1, Figure 1

This figure is a condensed version of Figures 10.1 and 10.2, so the supplemental information for those figures applies to this set of panels too.

## FAQ 10.2, Figure 1

### Data

One run each of the historical and RCP8.5 simulations is used from 24 CMIP5 models. The models are ACCESS1.0, CCSM4, CNRM CM5, CSIRO Mk3.6.0, CanESM2, EC EARTH, FGOALS g2, FGOALS s2, GFDL CM3, GFDL ESM2G, GFDL ESM2M, GISS E2 R, HadGEM2 CC, HadGEM2 ES, IPSL CM5A LR, IPSL CM5A MR, MIROC ESM CHEM, MIROC ESM, MIROC5, MPI ESM LR, MRI CGCM3, NorESM1 M, bcc csm1.1, inmcm4.

### Method

The primary test on summer surface temperature is applied using 30-year moving windows at 10-year steps, starting with 1900–1929 as a baseline and ending in 2070–2099 for the RCP8.5 model runs. This procedure is applied to each model and grid cell. The local warming is considered statistically significant when a Kolmogorov–Smirnov test rejects with 95% significance that the samples of the two 30-year windows are drawn from the same distribution. The last year of the moving window is taken as the year of emergence in one model. Changes are considered significant in the year when the signal is detected in 80% of the models. This procedure is done for each grid point. The year is then used to estimate the corresponding global temperature change based on the historical and RCP8.5 simulation in each model.

## References

Aldrin, M., M. Holden, P. Guttorp, R. B. Skeie, G. Myhre, and T. K. Berntsen, 2012: Bayesian estimation of climate sensitivity based on a simple climate model fitted to observations of hemispheric temperatures and global ocean heat content. *Environmetrics*, **23**, 253–271.

Annan, J. D., and J. C. Hargreaves, 2006: Using multiple observationally-based constraints to estimate climate sensitivity. *Geophys. Res. Lett.*, **33**, L06704.

Annan, J. D., J. C. Hargreaves, R. Ohgaito, A. Abe-Ouchi, and S. Emori, 2005: Efficiently constraining climate sensitivity with ensembles of paleoclimate simulations. *Sci. Online Lett. Atmos. (SOLA)*, **1**, 181–184.

Balan Sarojini, B., P. Stott, E. Black, and D. Polson, 2012 Fingerprints of changes in annual and seasonal precipitation from CMIP5 models over land and ocean. *Geophys. Res. Lett.*, **39**, L23706.

Bender, F. A. M., A. M. L. Ekman, and H. Rodhe, 2010: Response to the eruption of Mount Pinatubo in relation to climate sensitivity in the CMIP3 models. *Clim. Dyn.*, **35**, 875–886.

Brohan, P., J. J. Kennedy, I. Harris, S. F. B. Tett, and P. D. Jones, 2006: Uncertainty estimates in regional and global observed temperature changes: A new data set from 1850. *J. Geophys. Res. Atmos.*, **111**, D12106.

Cavalieri, D. J., and C. L. Parkinson, 2012: Arctic sea ice variability and trends, 1979–2010, *Cryosphere*, **6**, 881–889.

Chylek, P., and U. Lohmann, 2008: Aerosol radiative forcing and climate sensitivity deduced from the last glacial maximum to Holocene transition. *Geophys. Res. Lett.*, **35**, L04804.

Crowley, T. J., G. Zielinski, B. Vinther, R. Udisti, K. Kreutzs, J. Cole-Dai, and E. Castellano, 2008: Volcanism and the Little Ice age. *PAGES News*, **16**, 22–23.

Dee, D. P., et al., 2011: The ERA-Interim reanalysis: configuration and performance of the data assimilation system. *Q. J. R. Meteor. Soc.*, **137**, 553–597.

Domingues, C., J. Church, N. White, P. Gleckler, S. Wijffels, P. Barker, and J. Dunn, 2008: Improved estimates of upper-ocean warming and multi-decadal sea-level rise. *Nature*, **453**, 1090–1093.

Durack, P., S. Wijffels, and R. Matear, 2012: Ocean salinities reveal strong global water cycle intensification during 1950 to 2000. *Science*, **336**, 455–458.

Eyring, V., et al., 2013: Long-term changes in tropospheric and stratospheric ozone and associated climate impacts in CMIP5 simulations. *J. Geophys. Res. Atmos.*, doi:10.1002/jgrd.50316.

Folland, C. K., et al., 2013 High predictive skill of global surface temperature a year ahead. *Geophys. Res. Lett.*, **40**, 761–767.

Forster, P. M., T. Andrews, P. Good, J. M. Gregory, L. S. Jackson, and M. Zelinka, 2013 Evaluating adjusted forcing and model spread for historical and future scenarios in the CMIP5 generation of climate models. *J. Geophys. Res. Atmos.*, **118**, 1139–1150.

Forster, P. M. D., and J. M. Gregory, 2006: The climate sensitivity and its components diagnosed from Earth Radiation Budget data. *J. Clim.*, **19**, 39–52.

Frame, D. J., D. A. Stone, P. A. Stott, and M. R. Allen, 2006: Alternatives to stabilization scenarios. *Geophys. Res. Lett.*, **33**, L14707.

Frame, D. J., B. B. B. Booth, J. A. Kettleborough, D. A. Stainforth, J. M. Gregory, M. Collins, and M. R. Allen, 2005: Constraining climate forecasts: The role of prior assumptions. *Geophys. Res. Lett.*, **32**, L09702.

Gao, C., A. Robock, and C. Ammann, 2008: Volcanic forcing of climate over the past 1500 years: An improved ice core-based index for climate models. *J. Geophys. Res. Atmos.*, **113**, D23111.

Gillett, N. A., and J. C. Fyfe, 2013: Annular Mode change in the CMIP5 simulations. *Geophys. Res. Lett.*, **40**, 1189–1193.

Gillett, N. P., V. K. Arora, G. M. Flato, J. F. Scinocca, and K. von Salzen, 2012: Improved constraints on 21st-century warming derived using 160 years of temperature observations. *Geophys. Res. Lett.*, **39**, L01704.

Gillett, N. P., V. K. Arora, D. Matthews, P. A. Stott, and M. R. Allen, 2013 Constraining the ratio of global warming to cumulative CO2 emissions using CMIP5 simulations. *J. Clim.*, doi:10.1175/JCLI-D-12-00476.1.

Gleckler, P. J., et al., 2012: Human-induced global ocean warming on multidecadal timescales. *Nature Clim. Change*, **2**, 524–529.

Gong, D., and S. Wang, 1999: Definition of Antarctic oscillation index. *Geophys. Res. Lett.*, **26**, 459–462.

Goosse, H., J. Guiot, M. E. Mann, S. Dubinkina, and Y. Sallaz-Damaz, 2012a: The medieval climate anomaly in Europe: Comparison of the summer and annual mean signals in two reconstructions and in simulations with data assimilation. *Global Planet. Change*, **84–85**, 35–47.

Goosse, H., et al., 2012b: The role of forcing and internal dynamics in explaining the "Medieval Climate Anomaly'. *Clim. Dyn.*, **39**, 2847–2866.

Gregory, J. M., 2000: Vertical heat transports in the ocean and their effect an time-dependent climate change. *Clim. Dyn.*, **16**, 501–515.

Gregory, J. M., and P. M. Forster, 2008: Transient climate response estimated from radiative forcing and observed temperature change. *J. Geophys. Res. Atmos.*, **113**, D23105.

Gregory, J. M., R. J. Stouffer, S. C. B. Raper, P. A. Stott, and N. A. Rayner, 2002: An observationally based estimate of the climate sensitivity. *J. Clim.*, **15**, 3117–3121.

Haimberger, L., C. Tavolato, and S. Sperka, 2012: Homogenization of the global radiosonde temperature dataset through combined comparison with reanalysis background series and neighboring stations. *J. Clim.*, **25**, 8108–8131.

Hargreaves, J. C., J. D. Annan, M. Yoshimori, and A. Abe-Ouchi, 2012: Can the Last Glacial Maximum constrain climate sensitivity? *Geophys. Res. Lett.*, **39**, L24702.

Harris, G. R., D. M. H. Sexton, B. B. B. Booth, M. Collins, and J. M. Murphy, 2013: Probabilistic projections of transient climate change. *Clim. Dyn.*, doi:10.1007/s00382-012-1647-y.

Hegerl, G., J. Luterbacher, F. Gonzalez-Rouco, S. F. B. Tett, T. Crowley, and E. Xoplaki, 2011: Influence of human and natural forcing on European seasonal temperatures. *Nature Geosci.*, **4**, 99–103.

Hegerl, G. C., T. J. Crowley, W. T. Hyde, and D. J. Frame, 2006: Climate sensitivity constrained by temperature reconstructions over the past seven centuries. *Nature*, **440**, 1029–1032.

Hegerl, G. C., et al., 2010: Good practice guidance paper on detection and attribution related to anthropogenic climate change. In: *Meeting Report of the Intergovernmental Panel on Climate Change Expert Meeting on Detection and Attribution of Anthropogenic Climate Change* [T. F. Stocker, et al. (eds.)]. IPCC Working Group I Technical Support Unit, University of Bern, Bern, Switzerland, 8 pp.

Held, I. M., M. Winton, K. Takahashi, T. Delworth, F. R. Zeng, and G. K. Vallis, 2010: Probing the fast and slow components of global warming by returning abruptly to preindustrial forcing. *J. Clim.*, **23**, 2418–2427.

Helm, K. P., N. L. Bindoff, and J. A. Church, 2010: Changes in the global hydrological-cycle inferred from ocean salinity. *Geophys. Res. Lett.*, **37**, L18701.

Holden, P. B., N. R. Edwards, K. I. C. Oliver, T. M. Lenton, and R. D. Wilkinson, 2010: A probabilistic calibration of climate sensitivity and terrestrial carbon change in GENIE-1. *Clim. Dyn.*, **35**, 785–806.

Hu, Y. Y., L. J. Tao, and J. P. Liu, 2013: Poleward expansion of the Hadley circulation in CMIP5 simulations. *Adv. Atmos. Sci.*, **30**, 790–795.

Hurtt, G. C., et al., 2009: Harmonization of global land-use scenarios for the period 1500–2100 for IPCC-AR5. *Integrat. Land Ecosyst. Atmos. Process. Study (iLEAPS) Newslett.*, **7**, 6–8.

Imbers, J., A. Lopez, C. Huntingford, and M. R. Allen, 2013: Testing the robustness of the anthropogenic climate change detection statements using different empirical models. *J. Geophys. Res. Atmos.*, doi:10.1002/jgrd.50296.

IPCC, 2012: *Managing the Risks of Extreme Events and Disasters to Advance Climate Change Adaptation. A Special Report of Working Groups I and II of the Intergovernmental Panel on Climate Change* [Field, C.B., et al. (eds.)]. Cambridge University Press, Cambridge, UK, and New York, NY, USA, 582 pp.

Ishii, M., and M. Kimoto, 2009: Reevaluation of historical ocean heat content variations with time-varying XBT and MBT depth bias corrections. *J. Oceanogr.*, **65**, 287–299.

Ishii, M., M. Kimoto, K. Sakamoto, and S.-I. Iwasaki, 2006: Steric sea level changes estimated from historical subsurface temperature and salinity analyses. *J. Oceanogr.*, **62**, 155–170.

Jones, G. S., S. F. B. Tett, and P. A. Stott, 2003: Causes of atmospheric temperature change 1960–2000: A combined attribution analysis. *Geophys. Res. Lett.*, **30**, 1228.

Jones, G. S., P. A. Stott, and N. Christidis, 2013 Attribution of observed historical near surface temperature variations to anthropogenic and natural causes using CMIP5 simulations. *J. Geophys. Res. Atmos.*, doi:10.1002/jgrd.50239.

Jungclaus, J. H., et al., 2010: Climate and carbon-cycle variability over the last millennium. *Clim. Past*, **6**, 723–737.

Kaplan, J. O., K. M. Krumhardt, and N. Zimmermann, 2009: The prehistoric and preindustrial deforestation of Europe. *Quat. Sci. Rev.*, **28**, 3016–3034.

Kaufmann, R. K., H. Kauppi, and J. H. Stock, 2006: Emission, concentrations, & temperature: A time series analysis. *Clim. Change*, **77**, 249–278.

Kaufmann, R. K., H. Kauppi, M. L. Mann, and J. H. Stock, 2011: Reconciling anthropogenic climate change with observed temperature 1998–2008. *Proc. Natl. Acad. Sci. U.S.A.*, **108**, 11790–11793.

Kay, A. L., S. M. Crooks, P. Pall, and D. A. Stone, 2011: Attribution of Autumn/Winter 2000 flood risk in England to anthropogenic climate change: A catchment-based study. *J. Hydrol.*, **406**, 97–112.

Knutson, T. R., F. Zeng, and A. T. Wittenberg, 2013: Multi-model assessment of regional surface temperature trends. *J. Clim.*, doi:10.1175/JCLI-D-12-00567.1.

Knutti, R., and L. Tomassini, 2008: Constraints on the transient climate response from observed global temperature and ocean heat uptake. *Geophys. Res. Lett.*, **35**, L09701.

Knutti, R., T. F. Stocker, F. Joos, and G.-K. Plattner, 2002: Constraints on radiative forcing and future climate change from observations and climate model ensembles. *Nature*, **416**, 719–723.

Knutti, R., G. A. Meehl, M. R. Allen, and D. A. Stainforth, 2006: Constraining climate sensitivity from the seasonal cycle in surface temperature. *J. Clim.*, **19**, 4224–4233.

Koehler, P., R. Bintanja, H. Fischer, F. Joos, R. Knutti, G. Lohmann, and V. Masson-Delmotte, 2010: What caused Earth's temperature variations during the last 800,000 years? Data-based evidence on radiative forcing and constraints on climate sensitivity. *Quat. Sci. Rev.*, **29**, 129–145.

Kopp, G., and J. L. Lean, 2011: A new, lower value of total solar irradiance: Evidence and climate significance. *Geophys. Res. Lett.*, **38**, L01706.

Lanzante, J. R., 1996: Resistant, robust and non-parametric techniques for the analysis of climate data: Theory and examples, including applications to historical radiosonde station data. *Int. J. Climatol.*, **16**, 1197–1226.

Lean, J. L., and D. H. Rind, 2008: How natural and anthropogenic influences alter global and regional surface temperatures: 1889 to 2006. *Geophys. Res. Lett.*, **35**, L18701.

Lean, J. L., and D. H. Rind, 2009: How will Earth's surface temperature change in future decades? *Geophys. Res. Lett.*, **36**, L15708.

Levitus, S., J. Antonov, and T. Boyer, 2005: Warming of the world ocean, 1955–2003. *Geophys. Res. Lett.*, **32**, L02604.

Levitus, S., J. I. Antonov, T. P. Boyer, R. A. Locarnini, H. E. Garcia, and A. V. Mishonov, 2009: Global ocean heat content 1955–2008 in light of recently revealed instrumentation problems. *Geophys. Res. Lett.*, **36**, L07608.

Levitus, S., et al., 2012: World ocean heat content and thermosteric sea level change (0–2000 m), 1955–2010. *Geophys. Res. Lett.*, **39**, L10603.

Lewis, N., 2013: An objective Bayesian, improved approach for applying optimal fingerprint techniques to estimate climate sensitivity. *J. Clim.*, doi:10.1175/JCLI-D-12-00473.1.

Libardoni, A. G., and C. E. Forest, 2011: Sensitivity of distributions of climate system properties to the surface temperature dataset. *Geophys. Res. Lett.*, **38**, L22705.

Libardoni, A. G., and C. E. Forest, 2013: Correction to "Sensitivity of distributions of climate system properties to the surface temperature dataset". *Geophys. Res. Lett.*, doi:10.1002/grl.50480.

Lin, B., et al., 2010: Estimations of climate sensitivity based on top-of-atmosphere radiation imbalance. *Atmos. Chem. Phys.*, **10**, 1923–1930.

Lindzen, R. S., and Y. S. Choi, 2011: On the observational determination of climate sensitivity and its implications. *Asia-Pacif. J. Atmos. Sci.*, **47**, 377–390.

Lockwood, M., 2008: Recent changes in solar outputs and the global mean surface temperature. III. Analysis of contributions to global mean air surface temperature rise. *Proc. R. Soc. A*, **464**, 1387–1404.

Lott, F. C., et al., 2013: Models versus radiosondes in the free atmosphere: A new detection and attribution analysis of temperature. *J. Geophys. Res. Atmos.*, **118**, 2609–2619.

Luterbacher, J., D. Dietrich, E. Xoplaki, M. Grosjean, and H. Wanner, 2004: European seasonal and annual temperature variability, trend, and extremes since 1500. *Science*, **303**, 1499–1503.

MacFarling Meure, C., et al., 2006: Law Dome CO(2), CH(4) and N(2)O ice core records extended to 2000 years BP. *Geophys. Res. Lett.*, **33**, L14810.

Mann, M. E., et al., 2009: Global signatures and dynamical origins of the Little Ice age and medieval climate anomaly. *Science*, **326**, 1256–1260.

Mears, C. A., and F. J. Wentz, 2009: Construction of the remote sensing systems V3.2 atmospheric temperature records from the MSU and AMSU microwave sounders. *J. Atmos. Ocean. Technol.*, **26**, 1040–1056.

Meinshausen, M., et al., 2009: Greenhouse-gas emission targets for limiting global warming to 2 degrees C. *Nature*, **458**, 1158–U96.

Min, S.-K., X. B. Zhang, and F. Zwiers, 2008: Human-induced arctic moistening. *Science*, **320**, 518–520.

Min, S.-K., X. Zhang, F. W. Zwiers, and G. C. Hegerl, 2011: Human contribution to more intense precipitation extremes. *Nature*, **470**, 378–381.

Morak, S., G. C. Hegerl, and N. Christidis, 2013: Detectable changes in the frequency of temperature extremes. *J. Clim.*, **26**, 1561–1574.

Morice, C. P., J. J. Kennedy, N. A. Rayner, and P. D. Jones, 2012: Quantifying uncertainties in global and regional temperature change using an ensemble of observational estimates: The HadCRUT4 data set. *J. Geophys. Res. Atmos.*, **117**, D08101.

Murphy, D. M., S. Solomon, R. W. Portmann, K. H. Rosenlof, P. M. Forster, and T. Wong, 2009: An observationally based energy balance for the Earth since 1950. *J. Geophys. Res. Atmos.*, **114**, D17107.

North, G. R., and M. J. Stevens, 1998: Detecting climate signals in the surface temperature record. *J. Clim.*, **11**, 563–577.

Olson, R., R. Sriver, M. Goes, N. M. Urban, H. D. Matthews, M. Haran, and K. Keller, 2012: A climate sensitivity estimate using Bayesian fusion of instrumental observations and an Earth System model. *J. Geophys. Res. Atmos.*, **117**, D04103.

Otto, A., et al., 2013: Energy budget constraints on climate response. *Nature Geosci.*, **6**, 415–416.

Otto, F. E. L., N. Massey, G. J. van Oldenborgh, R. G. Jones, and M. R. Allen, 2012: Reconciling two approaches to attribution of the 2010 Russian heat wave. *Geophys. Res. Lett.*, **39**, L04702.

Padilla, L. E., G. K. Vallis, and C. W. Rowley, 2011: Probabilistic estimates of transient climate sensitivity subject to uncertainty in forcing and natural variability. *J. Clim.*, **24**, 5521–5537.

Paleosens Members, 2012: Making sense of palaeoclimate sensitivity. *Nature*, **491**, 683–691.

Pall, P., et al., 2011: Anthropogenic greenhouse gas contribution to UK autumn flood risk. *Nature*, **470**, 382–385.

Parker, D., C. Folland, A. Scaife, J. Knight, A. Colman, P. Baines, and B. Dong, 2007: Decadal to multidecadal variability and the climate change background. *J. Geophys. Res. Atmos.*, **112**, D18115.

Parkinson, C. L., and D. J. Cavalieri, 2012: Antarctic sea ice variability and trends, 1979–2010, *Cryosphere*, **6**, 871–880.

Pierce, D.W., P. J.Gleckler, T. P. Barnett, B. D. Santer, and P. J. Durack, 2012: The fingerprint of humaninduced changes in the ocean's salinity and temperature fields. *Geophys. Res. Lett*., **39**, L21704.

Piani, C., D. J. Frame, D. A. Stainforth, and M. R. Allen, 2005: Constraints on climate change from a multi-thousand member ensemble of simulations. *Geophys. Res. Lett.*, **32**, L23825.

Polson, D., G. C. Hegerl, X. Zhang, and T. J. Osborn, 2013: Causes of robust seasonal land precipitation changes. *J. Clim.*, doi:10.1175/JCLI-D-12-00474.1.

Pongratz, J., C. Reick, T. Raddatz, and M. Claussen, 2008: A reconstruction of global agricultural areas and land cover for the last millennium. *Global Biogeochem. Cycles*, **22**, GB3018.

Ribes, A., and L. Terray, 2013: Application of regularised optimal fingerprint analysis for attribution. Part II: Application to global near-surface temperature *Clim. Dyn.*, doi:10.1007/s00382-013-1736-6.

Rogelj, J., M. Meinshausen, and R. Knutti, 2012: Global warming under old and new scenarios using IPCC climate sensitivity range estimates. *Nature Clim. Change*, **2**, 248–253.

Santer, B. D., et al., 2013: Identifying human influences on atmospheric temperature. *Proc. Natl. Acad. Sci. U.S.A.*, **110**, 26–33.

Sato, M., J. E. Hansen, M. P. McCormick, and J. B. Pollack, 1993: Stratospheric aerosol optical depth, 1850–1990. *J. Geophys. Res. Atmos.*, **98**, 22987–22994.

Schmidt, G., et al., 2012: Climate forcing reconstructions for use in PMIP simulations of the last millennium (v1.1). *Geoscientif. Model Dev.*, **5**, 185–191.

Schmittner, A., et al., 2011: Climate sensitivity estimated from temperature reconstructions of the last glacial maximum. *Science*, **334**, 1385–1388.

Schneider von Deimling, T., H. Held, A. Ganopolski, and S. Rahmstorf, 2006: Climate sensitivity estimated from ensemble simulations of glacial climate. *Clim. Dyn.*, **27**, 149–163.

Schurer, A., G. Hegerl, M. E. Mann, S. F. B. Tett, and S. J. Phipps, 2013: Separating forced from chaotic climate variability over the past millennium. *J. Clim.*, doi:10.1175/JCLI-D-12-00826.1.

Schwartz, S. E., 2012: Determination of Earth's transient and equilibrium climate sensitivities from observations over the twentieth century: Strong dependence on assumed forcing. *Surv. Geophys.*, **33** 745–777.

Sexton, D. M. H., J. M. Murphy, M. Collins, and M. J. Webb, 2012: Multivariate probabilistic projections using imperfect climate models part I: outline of methodology. *Clim. Dyn.*, **38**, 2513–2542.

Skeie, R. B., T. K. Berntsen, G. Myhre, K. Tanaka, M. M. Kvalevåg, and C. R. Hoyle, 2011: Anthropogenic radiative forcing time series from pre-industrial times until 2010. *Atmos. Chem. Phys.*, **11**, 11827–11857.

Steinhilber, F., J. Beer, and C. Froehlich, 2009: Total solar irradiance during the Holocene. *Geophys. Res. Lett.*, **36**, L19704.

Stott, P. A., and C. E. Forest, 2007: Ensemble climate predictions using climate models and observational constraints. *Philos. Trans. R. Soc. A*, **365**, 2029–2052.

Stott, P. A., and G. S. Jones, 2012: Observed 21st century temperatures further constrain decadal predictions of future warming. *Atmos. Sci. Lett.*, **13**, 151–156.

Stott, P. A., J. F. B. Mitchell, M. R. Allen, T. L. Delworth, J. M. Gregory, G. A. Meehl, and B. D. Santer, 2006: Observational constraints on past attributable warming and predictions of future global warming. *J. Clim.*, **19**, 3055–3069.

Taylor, K. E., R. J. Stouffer, and G. A. Meehl, 2012: An overview of CMIP5 and the experiment design. *Bull. Am. Meteorol. Soc.*, **93**, 485–498.

Terray, L., L. Corre, S. Cravatte, T. Delcroix, G. Reverdin, and A. Ribes, 2012: Near-surface salinity as nature's rain gauge to detect human influence on the tropical water cycle. *J. Clim.*, **25**, 958–977.

Thorne, P. W., J. R. Lanzante, T. C. Peterson, D. J. Seidel, and K. P. Shine, 2011: Tropospheric temperature trends: history of an ongoing controversy. *WIREs Clim. Change*, **2**, 66–88.

Thorne, P. W., D. E. Parker, S. F. B. Tett, P. D. Jones, M. McCarthy, H. Coleman, and P. Brohan, 2005: Revisiting radiosonde upper air temperatures from 1958 to 2002. *J. Geophys. Res. Atmos.*, **110**, D18105

Tomassini, L., P. Reichert, R. Knutti, T. F. Stocker, and M. E. Borsuk, 2007: Robust bayesian uncertainty analysis of climate system properties using Markov chain Monte Carlo methods. *J. Clim.*, **20**, 1239–1254.

Tung, K. K., J. S. Zhou, and C. D. Camp, 2008: Constraining model transient climate response using independent observations of solar-cycle forcing and response. *Geophys. Res. Lett.*, **35** L17707.

Uppala, S. M., et al., 2005: The ERA-40 re-analysis. *Q. J. R. Meteor. Soc.*, **131**, 2961–3012.

Vieira, L. E. A., S. K. Solanki, N. A. Krivova, and I. Usoskin, 2011: Evolution of the solar irradiance during the Holocene. *Astron. Astrophys.*, **531**, A6.

Wang, M., and J. E. Overland, 2012: A sea ice free summer Arctic within 30 years: An update from CMIP5 models. *Geophys. Res. Lett.*, **39**, L18501.

Wang, Y. M., J. L. Lean, and N. R. Sheeley, 2005: Modeling the sun's magnetic field and irradiance since 1713. *Astrophys. J.*, **625**, 522–538.

Zhang, X. B., et al., 2007: Detection of human influence on twentieth-century precipitation trends. *Nature*, **448**, 461–465.

Zhang, X. D., 2010: Sensitivity of arctic summer sea ice coverage to global warming forcing: towards reducing uncertainty in arctic climate change projections. *Tellus A*, **62**, 220–227.

Zwiers, F. W., X. Zhang, and Y. Feng, 2011: Anthropogenic influence on long return period daily temperature extremes at regional scales. *J. Clim.*, **24**, 881–892.